Atmos. Meas. Tech. Discuss., 5, 6083–6145, 2012
www.atmos-meas-tech-discuss.net/5/6083/2012/
doi:10.5194/amtd-5-6083-2012

Atmospheric Measurement Techniques Discussions

Retrieval of aerosol microphysical and optical properties above liquid clouds from POLDER/PARASOL polarization measurements

F. Waquet, C. Cornet, J.-L. Deuzé, O. Dubovik, F. Ducos, P. Goloub, M. Herman, T. Lapionak, L. Labonnote, J. Riedi, D. Tanré, F. Thieuleux, and C. Vanbauce

Laboratoire d'Optique Atmosphérique, CNRS-INSU – UMR8518, Université Lille 1, Villeneuve d'Ascq, France

Received: 20 July 2012 – Accepted: 31 July 2012 – Published: 27 August 2012

Correspondence to: F. Waquet (fabien.waquet@uni-lille1.fr)

Published by Copernicus Publications on behalf of the European Geosciences Union.

Abstract

Most of the current aerosol retrievals from passive sensors are restricted to cloud-free scenes, which strongly reduces our ability to monitor the aerosol properties at a global scale. The presence of Aerosols Above Clouds (AAC) affects the polarized light reflected by the cloud layer, as shown by the spaceborne measurements provided by the POlarization and Directionality of Earth Reflectances (POLDER) instrument. We present new developments that allow retrieving the properties of mineral dust particles when they are present above clouds. These particles do not much polarize light but strongly attenuate the polarized cloud bow generated by the beneath liquid cloud layer. The spectral attenuation can be used to qualitatively identify the nature of the particles (i.e. mineral dust particles or biomass burning aerosols) whereas the magnitude of the attenuation is related to the optical thickness of the aerosol layer. We provide accurate polarized radiance calculations for AAC scenes and evaluate the contribution of the POLDER polarization measurements for the simultaneous retrieval of the aerosol and clouds properties. We investigate various scenes with mineral dust particles and biomass burning aerosols above clouds. We found that the magnitude of the primary cloud bow cannot be accurately estimated with a plane parallel transfer radiative code. The errors for the modelling of the polarized cloud bow are between 5 and 8 % for homogenous cloudy scenes, as shown by a 3-D radiative transfer code. For clouds, our results confirm that the droplets size distribution is narrow in high latitude ocean regions and that the droplets effective radii retrieved from polarization measurements and from total radiance measurements are generally close for AAC scenes (departures smaller than 2 µm). For the aerosols, the POLDER polarization measurements are primarily sensitive to the particles load, size distribution, shape and real refractive index. An algorithm was developed to retrieve the Aerosol Optical Thickness (AOT) and the Angström exponent above clouds in an operational way. This method was applied to various regions of the world and time period. Large mean AOTs above clouds at 0.865 µm (> 0.3) are retrieved for oceanic regions near the coasts of South Africa and

AMTD
5, 6083–6145, 2012

California (> 0.1) that correspond to biomass burning aerosols whereas even larger mean AOTs above clouds for mineral dust particles (> 0.6) are also retrieved near the coasts of Senegal (for June–August 2008). For these regions and time period, the direct AAC radiative forcing is likely to be significant. The final aim of this work is the global monitoring of the aerosol above clouds properties and the estimation of the direct aerosol radiative forcing in cloudy scenes.

1 Introduction

Aerosols directly affect the climate of the Earth by interacting with the solar and thermal infrared radiations. These atmospheric particles scatter the sunlight and reflect a part of it back into space. This effect is called the "direct aerosol effect" and cools the Earth's surface. By absorbing the solar light, absorbing aerosols further cool the surface but also warm the layer of the atmosphere where they reside. This modifies the vertical profile of temperature in the atmosphere, which affects the process of evaporation and cloud formation (Ackerman et al., 2000). This so-called "semi-direct aerosol effect", is currently not well quantified and might partially compensate for the aerosol direct effect at regional scale (Ramanathan et al., 1991). By acting as cloud condensation nuclei, these particles also have significant effects on the cloud microphysical properties (Bréon et al., 2002). Increasing aerosol concentrations results in an increase of cloud condensation nuclei available. This process can eventually cause a decrease in cloud droplets size, leading to an increase in cloud reflectivity (Twomey, 1977). This process is called the first "aerosol indirect effect" and contributes to cool the Earth. The reduction in cloud droplet size might also modify cloud lifetime and change precipitation efficiency (Rosenfeld, 2000). This process is referred as the second "aerosol indirect effect". Only the direct effect and the first indirect effect are currently quantified at a global scale with a level of knowledge qualified as medium and poor, respectively, according to the IPCC (2007).

AMTD
5, 6083–6145, 2012

In order to better understand the role of the aerosols on the Earth's climate, the spatial and temporal variability of their concentrations and microphysical properties have to be accurately measured and modelled. The aerosol microphysical properties are the particles size distribution, shape and composition. The aerosol size distribution is typically bimodal with a coarse and a fine mode (i.e. or accumulation mode). Fine mode particles are associated with size ranging between roughly 0.06 and 0.6 µm whereas coarse mode particles are larger than 0.6 µm (in radius). The aerosol microphysical properties exhibit a high variability at global scale since these particles are produced by various processes and sources and also because their properties evolve during the process of transport in the atmosphere. Anthropogenic aerosols can be directly emitted in the atmosphere (e.g. pollutants particles from industrial activities or biomass burning aerosols from man-made vegetation fires) or result from the conversion of anthropogenic gas into particles (e.g. sulphate aerosols). Natural processes also generate aerosols, as for instance, the mineral dust particles and the maritime aerosols (i.e. sea salt), which result from the mechanical action of the wind on the desert and ocean surfaces, respectively. Other natural aerosols include volcanic dust aerosols, pollens and ashes from wild vegetation fires. According to satellite passive observations, aerosols observed in industrial pollution regions and man-made vegetation fires regions mainly contribute to the fine mode whereas natural aerosols mainly contribute to the coarse mode with the mineral dust particles being the major contributor to the total amount of natural aerosols present in the troposphere (Kaufman et al., 2002).

Biomass burning fires aerosols are usually injected at high altitude in the atmosphere (> 6 km) and can be transported over considerable distance and overlie clouds. Man-made vegetation fires are frequent in South Africa between June and September (Tanré et al., 2001). Smoke plumes are uplifted above the continent at high altitude and, because of local meteorological conditions, transported primarily to the west over the Atlantic Ocean. Persistent decks of low-level stratiform cloud usually cover this part of the Atlantic Ocean during the same time period and the transport of biomass burning aerosols above clouds is frequent in this region. The transport of Saharan mineral dust

AMTD
5, 6083–6145, 2012

is also frequent across the Atlantic and dust plumes are regularly transported above low-level clouds off the coasts of Senegal (Haywood et al., 2003a). Other types of aerosols such as volcanic dust particles and pollutant particles (Hsu et al., 2003; Coddington et al., 2010) were also observed above clouds in other regions of the world. The most common observed situation corresponds to an elevated aerosol layer suspended above a low-level liquid water cloud. Aerosols Above Clouds (AAC) properties have not been studied much until today, as for their effects on climate. Biomass burning aerosols have strong absorption properties due to their high concentration in black carbon (Haywood and Boucher, 2000). When located above a cloud, strong absorbing particles reduce the brightness of the scene (i.e. the cloud albedo), which causes a local positive radiative forcing that contributes to warm the Earth. Regional studies of the AAC radiative forcing were achieved (Chand et al., 2009; Peters et al., 2011). However, this forcing is currently not constrained at a global scale, which explains that the estimation of the direct effect of biomass burning aerosols remains currently poorly quantified (Forster et al., 2007). The presence of biomass burning aerosols above clouds may also affect the dynamical evolution of clouds (Johnson et al., 2004). The induced effects could be a reduction in cloud top altitude and a cloud thickening. This might cause an enhancement of the cloud albedo (Wilcox et al., 2010).

In order to better quantify the aerosol radiative forcing in case of Aerosol Above Cloud (AAC) scenes, an accurate knowledge of the properties of the aerosols located above the clouds is required (primarily load, absorption and size). These properties allow estimating the aerosol optical parameters and their spectral dependence that controls the aerosol radiative forcing. The first optical parameter to be determined is the Aerosol Optical thickness (AOT) that is a measure of the radiation extinction due to particles scattering and absorption, integrated over the atmospheric column. Another optical parameter that is of importance for the estimation of the aerosol radiative forcing in cloudy scenes is the aerosol Single Scattering Albedo (SSA), which determines the amount of solar light that is absorbed by the particles (i.e. ratio of the scattering AOT to the total extinction AOT). If the impacts of human activities have to be estimated, the

AMTD
5, 6083–6145, 2012

nature of the particles must be identified (natural of anthropogenic), which requires the knowledge of the particles microphysics together with some information on their geographical origin. It is also required to determine the cloud albedo (Keil and Haywood, 2003), and to a lesser extent the respective vertical profiles of the aerosol and cloud layers.

Passive remote sensing by satellite provides observations at a global scale and on a daily basis and therefore constitutes a well-suited tool for aerosol (and cloud) monitoring (Kaufman et al., 2002). However, most of the current passive remote sensing techniques rely on the use of cloud-screening algorithms before retrieving the aerosols properties. This limits our ability to estimate the aerosol direct effects only to cloud-free scenes and restricts our capacity to estimate the total amount of aerosols. Furthermore, the presence of aerosols above clouds can also alter the accuracy of clouds properties retrievals performed from satellite passive sensors, which in turn may perturb the estimation of aerosols indirect effect (Haywood et al., 2004).

The detection of aerosols in cloudy scenes constitutes a new field of research in remote sensing. For passive remote sensing techniques, that use total radiance measurements, the main difficulty is to separate the radiative contribution of the aerosols from that of the clouds that is much stronger in magnitude than the aerosol one. Innovative methods based on the use of spectral radiance measurements were however developed and evaluated on some case studies. The approach described in De Graaf et al. (2007) uses measurements provided by the SCanning Imaging Absorption spectroMeter for Atmospheric CartograpHY (SCIAMACHY) instrument in a continuous broad spectral range (0.28–1.75 µm) to estimate the AOT and the aerosol SSA, under some assumptions made on the aerosol and cloud microphysical and optical properties. The method described by Torres et al. (2012) uses measurements provided by the Ozone Monitoring Instrument (OMI) radiometer in two Ultraviolet (UV) channels to simultaneously retrieve the aerosol and cloud optical thicknesses. Assumptions are also considered for the microphysical properties of the particles. Before retrieving the AOT,

AMTD
5, 6083–6145, 2012

the two methods rely on the use of an aerosol index to qualitatively detect the presence of UV-absorbing aerosols in cloudy scenes.

Active remote sensing techniques, based on the use of lidar systems, allow characterizing the vertical profile of the atmosphere (Winker et al., 2004). However, these instruments have limited spatial coverage, which is a clear disadvantage compared to passive sensors in terms of sampling events when aerosol layers are above clouds. Furthermore, current spaceborne lidar systems have limited capabilities to retrieve the aerosol burden without some priori knowledge on aerosol microphysics (Ackermann, 1998; Cattrall et al., 2005). An alternative method was recently developed for the Cloud-Aerosol Lidar with Orthogonal Polarization (CALIOP) spaceborne lidar that allows retrieving the optical thickness of any transparent layer (cirrus or aerosol) located above an opaque liquid water cloud. This method combines lidar backscattering coefficient measurements with linear depolarization ratio measurements and does not require assumptions on the aerosol microphysical properties (Hu et al., 2007).

Satellite passive remote sensing with polarization capabilities constitutes an alternative tool to study aerosols above clouds. In a general way, spectral angular polarized measurements are sensitive to particles load, size, shape and composition via sensitivity to the real part of the refractive index (Mishchenko et al., 1997). The presence of aerosols suspended above clouds significantly affects the polarized radiation reflected back to space by the cloud particles, as shown by the measurements provided by the POlarization and Directionality of Earth Reflectances (POLDER) instrument (Waquet et al., 2009a). An approximate formulation of the cloud-aerosol interaction was developed using single scattering approximation. The method was used to estimate the AOT of a biomass burning aerosols layer originated from South Africa and transported above stratiform low-level clouds in the South Atlantic Ocean. More recent works also outlined the importance of polarization measurements for the retrieval of the aerosol properties in cloudy scenes. Hasekamp et al. (2010) analyzes the contribution of multi-spectral, multi-angular total and polarized radiance measurements for the purpose of the simultaneous retrieval of the aerosol and clouds properties. This study investigates various

AMTD
5, 6083–6145, 2012

types of aerosol-cloud contaminated scenes (AAC scenes and scenes with fractional cloud cover mixed with aerosols). Knobelspiesse et al. (2011) analyzes the sensitivity of polarization measurements to aerosols properties for AAC scenes using the Aerosol Polarimetry Sensor (APS) instrument. The APS polarimeter was designed to acquire multi-angular, multi-spectral (0.41–2.2 µm) polarized measurements with a high polarimetric accuracy (Mishchenko et al., 2007), but the GLORY APS failed to reach orbit in 2011. An example of the aerosol optical and microphysical properties retrieved with the airborne simulator of the APS polarimeter is presented in Knobelspiesse et al. (2011), where the case study is relative to a layer of anthropogenic particles suspended above a marine stratocumulus cloud in the Gulf of Mexico.

Natural non-spherical coarse mode particles, such as mineral dust particles, do not much polarize light. For this reason, the method described in Waquet et al. (2009a) cannot be used to accurately retrieve the properties of mineral dust particles when they are present above clouds. In the present paper, we present new developments that allow retrieving the properties of mineral dust particles above clouds by using POLDER measurements acquired in the polarized cloud-bow. POLDER aboard Polarization and Anisotropy of Reflectances for Atmospheric Sciences Coupled with Observations from Lidar (PARASOL) was a part of the train of satellites, called A-train, between March 2006 and January 2010 and has acquired data in conjunction with multiple other passive and active sensors. Among those, the Moderate Resolution Imaging Spectroradiometer (MODIS) instrument provides high spatial resolution multi-spectral passive measurements (Salomonson et al., 1989) and the lidar CALIOP allows to characterize the vertical distribution of aerosols in atmosphere. We first study the particles properties observed for different transport events of mineral dust particles and biomass burning aerosols both in cloudy scenes and cloud-free ocean scenes using the conventional methods developed for the POLDER, MODIS and CALIOP instruments. In a second part, we evaluate the contribution of the POLDER polarized measurements for simultaneous retrieval of the aerosol and cloud properties. We present and evaluate different tools that allow to model the POLDER signal and retrieve the properties of the

AMTD
5, 6083–6145, 2012

observed particles. The advantage and limitations of each method are pointed out. The properties of the aerosols and clouds observed for various AAC scenes are depicted as accurately as possible. Finally, we compare our results with those of previous studies and conclude.

2 Observations

2.1 POLDER data

The data provided by POLDER instrument are the normalized total and polarized radiances, L and L_p. The normalized total radiance L is given by

$$L = \frac{\pi L^*}{E_s} \tag{1}$$

where L^* is the spectral radiance ($W m^{-2} sr^{-1} \mu m^{-1}$) and E_s is the spectral solar extraterrestrial irradiance ($W m^{-2} \mu m^{-1}$). The quantity L^* is related to the first Stokes parameter I and describes the total radiance measured by the instrument. L_p is given by

$$L_p = \pm \frac{\pi \sqrt{(Q^2 + U^2)}}{E_s} \tag{2}$$

where Q and U are the second and third Stokes parameters that characterize the linear polarization state of light. The Stokes parameters have the dimension of a spectral radiance ($W m^{-2} sr^{-1} \mu m^{-1}$). The plus or minus sign indicates that the direction of the scattered electric field is preferentially normal or parallel to the plan of scattering (Herman et al., 2005). Along the paper, when we discuss radiances, we will be referring to these normalized quantities. The polarized radiances are measured in three spectral

AMTD
5, 6083–6145, 2012

bands at 0.490, 0.670 and 0.865 µm. The POLDER instrument also acquires total radiance measurements in a number of other spectral bands (e.g. 0.765 and 1.02 µm) and provides images of the scene being viewed on a CCD matrix camera. The spatial resolution of POLDER is equal to $5.3 \times 6.2\,km^2$ at nadir. Because of the satellite motion and instrument design, the POLDER instrument can see the same scene from multiple angles (up to 16), allowing measuring the angular variability of these radiances. The viewing geometry is characterized by the scattering angle, Θ, that is the angle formed between the incident and scattered directions. We also introduce the sun zenith angle, θ_s, the view angle, θ_v, and relative azimuth angle, φ.

2.2 Aerosol and cloud properties from the A-TRAIN

We use the algorithm developed by Herman et al. (2005) to derive the aerosol properties over cloud-free ocean scenes. This method uses the total and polarization radiances acquired at 0.670 and 0.865 µm to derive several aerosol parameters at a resolution of 18.5 km × 18.5 km. The method mainly provides the aerosol optical thickness and the Angström exponent, a parameter indicative of the particles size. Through the rest of this paper, the Angström exponent, α, is defined as:

$$\alpha = -\ln\left(\frac{\tau_{0.670}}{\tau_{0.865}}\right) / \ln\left(\frac{0.670}{0.865}\right) \quad (3)$$

where $\tau_{0.670}$ and $\tau_{0.865}$ are the optical thicknesses retrieved by POLDER at 0.670 and 0.865 µm, respectively. The Angström exponent is of about 0.4 for mineral dust particles and it is typically larger than 1.8 for biomass burning aerosols (Dubovik et al., 2002). The AOT for the fine and coarse modes can also be retrieved as well as the fraction of non-spherical particles within the coarse mode. This latter parameter is only retrieved when the geometrical conditions are favourable. We refer to Herman et al. (2005) for more details regarding the assumptions used for the particles models and the modelling of the radiances.

AMTD
5, 6083–6145, 2012

In our analysis, we also use collocated cloud properties retrieved from MODIS and POLDER to characterize the cloudy scenes. We take advantage of the high spatial resolution retrieval capabilities of MODIS ($1 \times 1\,km^2$ at nadir) to estimate within each PARASOL pixel ($6 \times 6\,km^2$) the variability of the clouds properties. We compute a mean value for the cloud optical thickness (COT) and for the cloud droplet effective radius (REFF_CLD_M) as well as a standard deviation for each parameter (Δ_COT and Δ_REFF_CLD). We use the parameters extracted from the level-2 MODIS06 cloud product that are retrieved for ocean scenes by combining MODIS total radiances measurements acquired at 0.865 and 2.13 µm (Platnick et al., 2003).

We recall that the cloud parameters retrieved from passive radiometers may be biased for AAC scenes. For instance, Haywood et al. (2004) found biases for the cloud optical thickness retrieved by MODIS as large as 4 for a cloud with an optical thickness of 18 (the bias decreases to 2 for a cloud optical thickness of 12) and for a lofted biomass burning aerosols layer with an AOT of 0.2 at 0.86 µm.

The cloud phase is determined using an algorithm that combines the directional polarization measurements provided by POLDER with MODIS measurements acquired in the solar spectrum and thermal infrared (Riedi et al., 2010). The algorithm provides a semi-continuous phase index, referred as φ_CLD, ranging from confident liquid phase only to confident ice only ($0 < \varphi\_CLD < 200$).

The POLDER and MODIS instruments also provide various estimates of the cloud top heights. The comparison of these estimates provides valuable information for the detection of multi-layer situations (Waquet et al., 2009a). In the following, we use the cloud top altitude retrieved with: (i) the "IR cloud top pressure" method (z_c_IR) that uses MODIS measurements acquired in the thermal infrared (Menzel et al., 2006), (ii) the "Rayleigh cloud top pressure" method (z_c_Rayleigh), which uses the POLDER polarization signal of the molecules located above the clouds (Goloub et al., 1994) and (iii) the "apparent O_2 cloud pressure" method (z_c_O_2) that uses differential absorption measurements in the oxygen A-band of POLDER (Vanbauce et al., 2003). MODIS cloud pressure has been extracted from MYD06 cloud product that provides data at

AMTD
5, 6083–6145, 2012

a resolution of 5 km × 5 km (Platnick et al., 2003) and the POLDER data correspond to the RB2 (Radiative Budget Level 2) cloud products given at pixel resolution of 18.5 km × 18.5 km (Parol et al., 2004).

Finally, the CALIOP lidar data are used to characterize the vertical profile of the atmosphere along the A-train orbit track. We use the aerosol/cloud classification that corresponds to the Lidar Level 2 Vertical Feature Mask (VFM) Product (Vaughan et al., 2004).

2.3 Case studies of aerosols transport events

2.3.1 Biomass burning aerosols

Figure 1a is a true color composite image illustrating POLDER total radiance observations, acquired over the tropical southeast part of the Atlantic Ocean on the 4 August 2008. This image was produced using a combination of the POLDER spectral bands centred on 0.490 µm, 0.565 µm and 0.670 µm. The transport of biomass burning aerosols over clouds is expected in this region for this time period (e.g. Waquet et al., 2009a). The region is partially covered by clouds. The total Aerosol Optical Thickness (AOT) retrieved over cloud free pixels is reported in Fig. 1b. The largest AOTs (≈ 0.6) are observed over the cloud-free parts of the Gulf of Guinea. The Angström exponent is about 1 in this region, which indicates that the algorithm retrieves a bimodal size distribution. We assume that the algorithm is sensitive to two types of particles, the maritime aerosols (coarse mode particles) located in the boundary maritime layer and the biomass burning aerosols (mainly fine mode particles) located in the elevated layer.

We reported the CALIOP mask results in Fig. 1c. An aerosol layer is observed at altitude between 2 km and 4 km above low-level clouds for latitudes ranging between −8.5° and −21°. For latitudes larger than −8.5°, the lidar signal is too attenuated and the particles located in the lower atmosphere cannot be observed. The cloud top heights retrieved from passive observations are reported in Fig. 1c. We selected the POLDER and MODIS pixels which centers are the closest to the ones of the CALIOP pixels.

AMTD
5, 6083–6145, 2012

The anomalies observed between the three different estimates of the cloud top heights for latitudes larger than −20° are characteristic of AAC scenes with biomass burning aerosols (Waquet et al., 2009a). The "IR" and "Rayleigh" methods both largely overestimate the cloud top height with the largest biases observed on z_c_Rayleigh. The "apparent O_2 cloud pressure" appears to be not much perturbed by the aerosols layer and tends to slightly underestimate the true cloud top altitude. This method provides an estimate of the cloud top height that is intermediate between the geometric middle of the cloud layer and the cloud top height, which is what we expect for low-level single cloud layers (Ferlay et al., 2010). Most of clouds observed in the POLDER image shown in Fig. 1a correspond to low-level optically thick clouds (0.45 km < z_c_O_2 < 1.05 km, 3.0 < COT < 18.0) with a cloud thermodynamical phase index, φ_CLD, of about 10, which means high probability for liquid phase.

2.3.2 Mineral dust aerosols

We reported POLDER images acquired over the North Eastern tropical Atlantic Ocean on the 25 July 2008 and on the 4 August 2008, respectively in Figs. 2a and 3a, together with the lidar CALIOP traces. The presence of mineral dust particles above low-level clouds is expected in this region during the selected time period (De Graaf et al., 2007). The transport of mineral dust particles can be observed in cloudy scenes in Figs. 2a and 3a. An optically thick liquid low-level cloud can be observed (COT > 5. and z_c_O_2 < 0.4 km) for the July case. The cloud cover is more fractional and less optically thick for the August case. The AOTs retrieved by POLDER over cloud-free ocean scenes are reported in Figs. 2b and 3b. Strong AOT values can be observed, as large as 1.7, on the 25 July 2008. The Angström exponent is close to zero for both days indicating a size distribution dominated by the coarse mode particles. The fraction of non-sphericity is only available on the 25 July 2008 and indicates that the coarse mode mainly consists in non-spherical particles, which is perfectly consistent with origins of the aerosol layer.

AMTD
5, 6083–6145, 2012

The presence of mineral dust particles above clouds cannot be checked with the lidar data for the July case, since the optically thick cloud observed by POLDER is outside the CALIOP track (see Fig. 2c). The anomalies observed between the three different estimates of the cloud top heights remain qualitatively similar to that of an AAC scene with biomass burning aerosols (z_c-$O_2 < z_c$-IR $< z_c$-Rayleigh) with, however, smaller biases noted on z_c-Rayleigh, resulting from the lower polarization produced by non-spherical particles. For instance, the average values for z_c-O_2, z_c-IR and z_c-Rayleigh computed for box 3 in Fig. 2c are equal to 0.275, 2.75 and 3.45 km, respectively. The CALIOP mask results are shown in Fig. 2c. The CALIOP mask shows a complex situation with aerosols detected at different altitudes between the sea surface and 6 km that are potentially imbedded with some optically thin cloudy structures. We observe some abrupt variability in the CALIOP results that we assume to be artificial for the most parts since the CALIOP mask is sometimes subject to misclassification between aerosols and clouds layers, especially when dense dust layers are encountered (Chen et al., 2010).

The CALIOP results obtained for the case study on mineral dust particles acquired for the 4 August 2008 are reported in Fig. 3c, together with the cloud top height estimates retrieved from POLDER and MODIS. The dust plume is observed at altitudes between 2 km and 6 km above low-level clouds for latitudes ranging between 18° and 24°. The same layer is observed above a maritime boundary layer for latitudes ranging between 24° and 27.5°. The results obtained with the "Rayleigh" method are not available due to unfavourable geometric conditions (i.e. this method requires observations acquired at small scattering angles that are not available here). The results for z_c-O_2 and z_c-IR remain qualitatively similar to the ones obtained for the two previous cases.

2.4 Polarized signatures for AAC scenes

Figure 4a shows the angular polarized features typically observed for liquid clouds in pristine conditions. The measurements were sampled over the Atlantic Ocean, South-western of South Africa (roughly half way between South Africa and Antarctica)

AMTD
5, 6083–6145, 2012

to prevent any contamination by African aerosols. We segregated the POLDER data into boxes of 200 km × 200 km. We only selected pixels associated with clouds with optical thickness larger than 3., as simulations performed with a parallel transfer radiative plane model show that the polarized radiance reflected by the cloud is "saturated". It means that the polarized signal does not depend on the cloud optical thickness anymore. At 0.865 µm, we observe small levels of polarization at side scattering angles ($80^\circ < \Theta < 130^\circ$) and a strong peak of polarization around 140° that corresponds to the primary cloud-bow. A secondary sharp cloud-bow can also be observed around 150°. As the wavelength decreases from 0.865 µm to 0.49 µm, the polarized radiance increases at side scattering angles due to molecular scattering.

The areas selected illustrate the peculiar signature obtained for AAC scenes with biomass burning aerosols and mineral dust particles are, respectively shown in Figs. 1a (box 1) and 2a (box 3). For AAC scenes, an additional polarization signal at side scattering angles at 0.865 µm and 0.67 µm and a spectral attenuation of the primary cloud-bow magnitude can be observed. The excess of polarization is much larger for biomass burning aerosols than for mineral dust particles, particularly for 0.67 and 0.865 µm. This explains why the "Rayleigh method" strongly overestimates the cloud top height for AAC scenes with biomass burning aerosols. The spectral attenuation of the cloud-bow is also relevant of the particles type. Fine mode particles are associated with an AOT that rapidly decreases as the wavelength increases (Angström exponent of about 2.) whereas coarse mode particles are associated with a rather spectrally flat AOT (Angström exponent of about 0.). As a consequence, the attenuation of the primary cloud-bow is spectrally dependent (i.e. colourful) for biomass-burning AAC and almost spectrally neutral for mineral dust particles. For this latter case, the primary bow is strongly attenuated but can be still observed around 140° (see Fig. 4c), which confirms that a large amount of coarse mode particles was transported above the clouds on the 25 July 2008.

AMTD
5, 6083–6145, 2012

3 Simultaneous retrieval of the aerosol and cloud properties: the "hyper-pixel method"

3.1 Strategy

The algorithm described in Waquet et al. (2009a) was oriented for the retrieval of fine mode particles properties above clouds. This method was therefore restricted to the use of observations acquired for scattering angles smaller than 130° where polarization measurements are highly sensitive to scattering by fine mode aerosols and only weakly sensitive to cloud microphysics. The cloud droplets distribution effective radius primarily drives the magnitude of the primary cloud-bow for a single layer cloud (Bréon et Goloub, 1998). This parameter must be therefore estimated or included in the retrieval process if the measurements acquired in the cloud bow have to be considered for the retrieval of the aerosol properties. The key parameter for the retrieval of the droplets effective radius is the knowledge of the angular locations of the primary and surnumerary cloud bows (Bréon et Goloub, 1998). Simulations of polarized radiance performed for AAC scenes show that the aerosol layer attenuates the magnitudes of all the cloud bows but does not modify their angular locations (see Fig. 5). We therefore conclude that the simultaneous retrieval of the aerosol properties and droplets effective radius is possible for AAC scenes, as long as the primary cloud bow remains visible (i.e. not too attenuated) and that enough angular polarized measurements are available.

3.2 Algorithm

The simultaneous retrieval of the aerosol and cloud properties is performed using an Optimal Estimation Method (OEM), similar as the one described in Waquet et al. (2009b). The particles properties are retrieved by comparing the measured and simulated polarized radiances and by adjusting the parameters in the particles models until the best match is found. The search for the best solution is achieved through the use of an iterative process. We use the Newton-Gauss iteration modified with

AMTD
5, 6083–6145, 2012

the Levenberg-Marquadt technique to ensure convergence. We refer to Waquet et al. (2009b) or to Rodgers (2000) for more details concerning the practical implementation of this procedure. The OEM is coupled with a radiative transfer code and a module that allows calculating the optical properties of the particles (described hereafter). This method provides a diagnostic error that accounts for the measurements' sensitivity to the retrieved parameters, the measurement's errors and the modelling's errors as well as any available a priori information. The retrieval error covariance matrix $\mathbf{C}_x$ is defined as :

$$\mathbf{C}_x = \left(\mathbf{C}_\mathrm{a}^{-1} + \mathbf{K}^T \cdot \mathbf{C}_\mathrm{T}^{-1} \cdot \mathbf{K}\right)^{-1}, \quad (4)$$

where $\mathbf{C}_\mathrm{T}$ is the total error covariance matrix and $\mathbf{C}_\mathrm{a}$ is the a priori error covariance matrix. $\mathbf{K}_i$ is the Jacobian matrix and is defined as:

$$\mathbf{K}_{ij} = \frac{\partial F_i(\boldsymbol{X})}{\partial \boldsymbol{X}_j}, \quad (5)$$

where $\boldsymbol{F}$ is the simulation vector and $\boldsymbol{X}$ is the vector of parameters. $\mathbf{K}$ is computed for each observation (i) and each parameter (j) and represents the sensitivity of the simulated polarized radiances to the particles parameters.

The square root of the diagonal elements of the error covariance matrix provides the standard deviation associated to each retrieved parameter. The error covariance matrices for the optical parameters are derived from the retrieved parameters and computed using Eq. (4) and the formula given in the Appendix A1.

3.3 Input data

3.3.1 "Hyper-pixel" data

The so-called "hyper-pixel" refers to POLDER data aggregated at a spatial scale of $200 \times 200\,\mathrm{km}^2$. It allows obtaining a homogeneous sampling of the scattering angle

AMTD
5, 6083–6145, 2012

that helps for the retrieval of detailled aerosol and cloud properties. This approach was initially used in Bréon et Goloub (1998) for the retrieval of cloud microphysical properties for a single cloud layer and it is adapted here for the purpose of the retrieving of the aerosol and cloud properties for AAC scenes.

Before the retrieval of the aerosol and cloud at the hyper-pixel scale, we first apply a retrieval method that works at the finest spatial POLDER resolution ($6 \times 6\,km^2$), such as the one described in Waquet et al. (2009a). It allows estimating the spatial variability of the AOT above clouds within the hyper-pixel and to only select homogenous pixels in terms of both aerosol and cloud properties. The variability of the atmospheric vertical profile within the hyper-pixel is also qualitatively estimated using the "apparent O_2 cloud pressure" and lidar data when available. Indeed, thin cirrus, multi-layers or broken clouds situations tend to increase the spatial variability of the observed apparent O_2 pressure.

We use a specific procedure for the aggregation of the data that is different than the one used in Bréon and Goloub (1998). We split the data using the polar coordinate system and subdivide the range of scattering sampled by POLDER into small intervals of 0.5°. A mean viewing geometry ($\underline{\theta_s}$,$\underline{\theta_v}$, $\underline{\varphi}$ and $\underline{\Theta}$) and a mean polarized radiance value are then computed for each 0.5° scattering angle interval using the corresponding information available at the $6 \times 6\,km^2$ spatial resolution. The scattering angle used to depict the angular behaviour of the mean polarized radiance is referred as $\underline{\Theta}^*$ and it is computed from the mean viewing geometry ($\underline{\theta_s}$,$\underline{\theta_v}$ and $\underline{\varphi}$).

Precautions must be taken for the calculation of the mean viewing geometry when the multiple scattering effects in the atmosphere have to be accounted for. The data associated with different viewing geometries (θ_v, φ) that correspond to the same value of scattering angle must be separately aggregated since these data show different values of polarized radiance, due to the effects of cloud multiple scattering. We apply a geometric criterion (i.e. $\left|\underline{\Theta}^* - \underline{\Theta}\right| < 0.1°$) that prevents to aggregate together data belonging to the same 0.5° scattering angle interval everthough they are associated with significant different viewing geometries.

AMTD
5, 6083–6145, 2012

An example of aggregated data is shown in Fig. 6. Two different "branches of scattering angle" are usually observed by POLDER when an area of $200 \times 200\,km^2$ is considered (e.g. $97^\circ < \Theta < 177^\circ$ and $157^\circ < \Theta < 177^\circ$ in Fig. 6a). In the retrieval algorithm, we consider only one "branch of scattering angle" for sake of simplicity. We select the branch associated with the widest range of scattering angles (e.g. $97^\circ < \Theta < 177^\circ$ in Fig. 6a). Figs. 6a and 6b show that this procedure allows to obtain rather smooth mean polarized radiances associated with a consistent mean viewing geometry.

3.3.2 Errors' measurements

The error's measurements are taken from Fougnie et al. (2007) and are used to fill out the total error covariance matrix. We consider a relative error of calibration of 2 % in the three polarized spectral bands. The polarization measurements are acquired by POLDER using a sequential rotation of polarizers oriented at 0, 60 and −60°. One of the measurements triplets at 0.67 µm was shown to be imperfect by construction, which tends to increase the noise in the polarized data acquired at this wavelength (see for instance Fig. 4a). The noise associated with the polarized radiances for cloudy scenes is estimated to be 2.5×10^{-3} at 0.49 µm and 0.865 µm and 5×10^{-3} at 0.67 µm. We assume that the different sources of errors are independent and the total covariance matrix is given by the sum of the different error covariance matrices.

3.4 Particles models and a priori information

A combination of two lognormal size distribution functions is assumed for the aerosols. A geometric mean radius and a standard deviation are used to describe each lognormal function (r_g and σ), where r_g is the geometric mean radius. The other retrieved parameters are the column number density of particles (N, in μm^{-2}), for both modes, and the complex refractive index ($m_r - m_i i$) that is assumed to be spectrally invariant and the same in both modes. The effective radius, r_{eff}, is related to the lognormal size distribution parameters using the formula given in the Appendix A2.

AMTD
5, 6083–6145, 2012

For non-spherical particles, we consider spheroid models with various aspect ratios to compute the optical properties of the aerosols (Mishchenko and Travis, 1994; Dubovik et al., 2006). We consider a mixture of spherical and non-spherical particles. The ratio of spherical particles over the total number of particles (SF) is included in the retrieval process for AAC scenes with mineral dust particles. The aspect ratios distribution for the non-spherical particles model is the one derived by Dubovik et al. (2006) from the analysis of the scattering matrix of mineral dust samples (Volten et al., 2001).

The cloud droplets size distribution is assumed to follow a gamma standard law, described by two parameters, the cloud droplets effective radius, $r_{\text{eff\_cld}}$, and the cloud droplets effective variance, $v_{\text{eff\_cld}}$, as defined in Hansen and Travis (1974). The real refractive index for cloud droplets, $m_{\text{r\_cld}}$, is retrieved in each spectral band. The imaginary refractive index for cloud droplets is less than 5×10^{-7} for the POLDER wavelengths (Hale et al., 1973) and it is therefore neglected in the calculations (held constant to 0). Angular polarization measurements are highly sensitive to the real refractive index of large spherical particles due to the presence of bows. We make clear that the droplets real refractive index is primarily included in the retrieval process to ensure an accurate modelling of the cloud bows (angular locations and magnitudes). The droplet effective variance is also included in the algorithm, since this parameter strongly impacts the magnitude of surnumerary cloud bows. The cloud droplets are modelled as spheres and their optical properties are therefore calculated using the Mie theory.

In Table 1, we provide the values of the a priori aerosol and cloud parameters ("starting point for $\boldsymbol{X}$") and the associated uncertainties ($\mathbf{C}_a$). The subscripts $_f$ and $_c$ respectively denote parameters that describe the fine mode and coarse mode aerosols. The number of retrieved parameters included in the OEM can be modified and the a priori information as well. If so, we provide the corresponding information in text.

AMTD
5, 6083–6145, 2012

3.5 Forward model

3.5.1 Transfer radiative code and particles vertical distribution

The polarized radiances are computed using the Successive Order of Scattering code (SOS) that accounts for the effects of multiple scattering under the assumption of the plane parallel atmosphere (Lenoble et al., 2007). The SOS code provides the usual three first Stokes parameters and allows including various atmospheric components that are separately described for the optical properties and the vertical profile. The vertical profile for the molecules is defined using a decreasing exponential law with a scale height of 8 km. The molecular optical thickness and the effects of molecular anisotropy are computed using the formulae given in Hansen and Travis (1974). The vertical profile of the aerosol layer is described using a Gaussian distribution function, defined by a standard deviation (0.75) and a mean altitude value, $z_$mean. The cloud droplets particles are assumed well mixed with the molecules between the surface and the cloud top height. The cloud base height is therefore located at 0 km. The cloud optical thickness is held constant to 5, which ensures that the polarized radiance reflected by the cloud layer is saturated. The mean altitude of the aerosol layer and the cloud top height are adjusted using the lidar data. When those are not available, we use the "apparent O_2 cloud pressure" to estimate the cloud top height and assume a mean altitude $z_$mean of 3.5 km for the AAC height. Then, we apply an empirical correction on $z_c\_O_2$, defined on the basis of our observations, which accounts for the fact that the "apparent O_2 cloud pressure" underestimates the cloud top height given by CALIOP. For instance, we used a correction of about 40 % for AAC scenes with mineral dust particles on the basis of the observations performed on the 4 August 2008 (see Fig. 3b between latitudes 19° and 23°).

AMTD
5, 6083–6145, 2012

3.5.2 Effects of phase function truncature

The SOS code requires a Legendre polynomial expansion of the phase matrix. The forward peak of the phase function (i.e. the P11 element of the phase matrix) is generally sharp for large particles such as cloud particles, which requires to increase the number of terms in the expansion of the phase matrix. A truncation procedure of the forward scattering peak is implemented in the SOS code (Potter, 1970; Nakajima and Tanaka, 1998). This procedure allows a faster modelling of the radiances. We however noted that this procedure introduces small errors in the modelling of the upwelling polarized radiance under specific circumstances that are encountered in this paper. Errors appear when large spherical particles are considered and when the polarized radiance is saturated (optical thickness > 3). Significant errors appear in the primary cloud bow region. The magnitude of the primary cloud-bow is overestimated by 7.5 % when the procedure of truncation is invoked. Calculations performed for a truncation applied to scattering angles between 0° and 16°, for a droplet effective radius of 10 µm, a droplet effective variance of 0.06, cloud optical thickness of 5 and a sun zenith angle of 37°. The reasons for this issue are not fully understood and the solving of this technical problem will be attempted in a future effort. In the retrieval algorithm, we use an exact 1-D modelling (no truncation) at the end of each step in the iteration to compare the observations to the simulations whereas the intermediate calculations (i.e. the Jacobian matrix elements) are performed using the approximation of truncature.

3.5.3 3-D cloud effects

It is well known that the homogeneous 1-D cloud assumption leads to errors in the retrieved cloud parameters from total visible radiance (Marshak and Davis, 2005). Cornet et al. (2009) show for a cirrus cloud with a Monte-Carlo radiative transfer code that biases exist also on polarized radiance. To assess the errors in our 1-D transfer radiative model, we compute 3-D and 1-D polarized radiance of a stratocumulus cloud with a mean optical thickness of 10 and an uniform effective radius of 10 µm and an effective

AMTD
5, 6083–6145, 2012

variance of 0.02. The heterogeneity parameter is 7 for the optical thickness (standard deviation associated with the mean optical thickness). The initial resolution of the radiative transfer simulation is $80 \times 80\,m^2$. The radiances are then spatially averaged at $10 \times 10\,km^2$ to simulate the observation of a sensor like POLDER. The differences between the 1-D and 3-D polarized reflectances in function of the scattering angle are presented in Fig. 7 for the three wavelengths used in the algorithm and for different sun angles. For most of the scattering angles, and for the case considered here, which does not include microphysical heterogeneity, the differences between the two polarized reflectances are small and inside the statistical error of the Monte-Carlo simulations (not plotted). Exceptions appears however in the forward direction for large sun angle and the cloud bow regions near 140°. Considering our algorithm, the differences, which may impact the most our retrieval, are those in the cloud-bow direction. The 1-D simulations systematically overestimate the ones that account for the 3-D cloud effects by about 5–8 %, depending on wavelength and geometry (θ_s, φ). Because for computing time reasons, it is pratically impossible to account for those 3-D effects in our retrieval procedure, we incorporated these errors into the total error covariance matrix ($\mathbf{C}_T$).

4 Sensitivity study and discussion

4.1 Biomass burning aerosols

The OEM algorithm is flexible and the number of retrieved parameters can be increased or decreased as needed. We did several tests with varying numbers of retrieved parameters in order to provide a sensitivity study. We first investigate the AAC scene with biomass burning aerosols, referred as box (1) in Fig. 1a. The solutions obtained for various retrieval schemes are reported in Table 2. The quantity ω_0 denotes the aerosol single scattering albedo. The quantity ε is the mean squared difference error term calculated between measured and simulated polarized radiances (see Appendix A3). This quantity gives a simple measure of the difference between measurements and

AMTD
5, 6083–6145, 2012

simulations, assuming a diagonal identity matrix for $\mathbf{C}_x$ (no weight) and no a priori knowledge. Note that the quantity ε is consistent with the definition of the error term considered in the less sophisticated retrieval method described in Sect. 5. Solution 1 includes the retrieval of the parameters of load and size for the fine particles and the microphysical parameters for the clouds particles. We consider spherical particles, which is a reasonable assumption for biomass burning aerosols. The value for the spherical fraction (SF) (spherical fraction of particles) indicated in Table 1 (0.5 ± 0.5) is therefore modified and held constant to 1. Solution 2 is the same as solution 1 but includes the retrieval of the properties of the coarse mode (load and size parameters). Solutions 1 and 2 both assume a weak absorption. Solution 3 is similar as solution 2 with in addition the retrieval of the imaginary part of the complex refractive index (i.e. absorption). Solution 4 is similar as solution 3 but includes the retrieval of the real part of the refractive index. The real and imaginary parts of the complex refractive index are assumed to be similar for both modes. For solution 5, we made assumptions for the coarse mode particles optical thickness (0.015 at 0.865 µm), the coarse mode particles effective radius ($r_{\text{eff\_c}} = 2.55\,\mu\text{m}$) and for the real refractive index ($m_r = 1.47$). Solution 5 is an attempt to reduce the space of solutions by limiting the number of retrieved parameters. We recall that the aerosol SSA depends on both particles absorption and size distribution. Then, any errors due to the assumptions made about the aerosol properties (e.g. for the size or the coarse mode AOT) directly affect the retrieval of the aerosol SSA.

Solution 1 allows to robustly model the POLDER data (not shown) and confirms that the polarized measurements are primarily sensitive to the fine mode scattering AOT and its spectral dependence as well as the cloud microphysical properties. The measurements are potentially sensitive to the aerosol Single Scattering albedo (SSA) since the polarization observed at side scattering angles is related to the scattering AOT whereas the effect of attenuation of the aerosol layer on the polarized light reflected by the cloud depends on the total (extinction) AOT. The algorithm shows some sensitivity to the aerosol SSA. We observed that the effect of the absorption on the polarized radiances is rather small but not negligible. Solution 4 includes the most degrees

AMTD
5, 6083–6145, 2012

of freedom in terms of retrieved aerosol microphysical parameters and retrieves an aerosol model for which the size distribution is dominated by fine mode particles (α of about 2.) associated with rather strong absorption properties (m_i of 0.017 ± 0.007). The standard deviation for each parameter is small, excepted for the coarse mode particles effective radius, which tends to indicate that the algorithm is sensitive to most of the parameters considered in solution 4. The least square error term ε is minimized for this solution. We however note that the other solutions (1, 2, 3, and 5) allow to accurately model the POLDER data (e.g. see Fig. 8a for solution 5) and shows rather similar low ε values. The retrieved AOTs at 0.865 µm are rather similar for all these solutions but differences appear for the aerosol microphysical parameters. For instance, the contribution of the coarse mode particles to the total AOT is larger for solution 2 than for solution 4 whereas the absorption is much smaller for solution 2 than for solution 4.

Solution 5 provides an estimate of the aerosol SSA equal to 0.815 (±0.045) at 0.865 µm, which is consistent with biomass burning aerosols in South Africa according to AERONET sun-photometers observations (Dubovik et al., 2002). The mean aerosol SSA is 0.80 ± 0.004 (at 0.87 µm) and the mean imaginary part of the complex refractive index is 0.021 ± 0.004, for biomass burning aerosols observed in the centre of South Africa (Zambia). Our estimate also agrees rather well with the one provided by Leahy et al. (2007), who found an aerosol single scattering albedo of 0.85 ± 0.02 (regional mean and uncertainty at 0.55 µm), on the basis of an updated analysis of remote and in situ measurements performed during the Southern African Regional Science Initiative 2000 (SAFARI). We also investigated another day in the same region in August 2008 for a scene with a retrieved AOT of 0.21 (±0.01) in biomass burning AAC and found an aerosol SSA of 0.91 (±0.05) at 0.865 µm with solution 5. It is impossible to tell if this variability observed from one case to another is due to a real change in the aerosol microphysical properties or due to the issue of multiple solutions in our retrievals. We note that a previous study suggested a higher value for the aerosol SSA (0.91 ± 0.04 at 0.55 µm) for SAFARI (Haywood et al., 2003b) and that some variability

AMTD
5, 6083–6145, 2012

in the degree of absorption of the biomass-burning aerosols is expected during the fire season in South Africa (Eck et al., 2003).

We reported the results obtained for two other "hyper-pixels" in Table 4 that both correspond to scenes with small AAC optical thickness. We used solution 5 to analyze both cases. Case (1) in Table 4 corresponds to an AAC scenes encountered for the case study on biomass burning aerosols that is referred as box (2) in Fig. 1a. Case (2) corresponds to the data acquired on the 18 August 2008 for clouds observed in pristine conditions between South Africa and Antarctica. The algorithm retrieves a small value of AOT for case (1) but still retrieves a size distribution dominated by small particles, which suggests a continental origin. The retrieved AOT is very small (0.022 ± 0.003) for case (2) and the type of particles then cannot be identified since the Angström exponent cannot be accurately retrieved anymore ($\alpha = 0.88 \pm 1.08$). Some difficulties in the modelling of the polarized radiances can be observed for case (1) for large scattering angles ($\approx 180^{\circ}$) that are not clearly understood (see Fig. 8c). We assume that it could be the result of the scene spatial heterogeneity. In a general way, we note that significant errors in the modelling of the polarized radiances appear in the cloud-bow region when the AAC optical thickness is small (see Fig. 8c and d) that are probably due to 3-D cloud effects. Nevertheless, these two latter results indicate that that the AAC optical thickness progressively decreases as we move away from South Africa and that solution 5 remains robust even when the AOT becomes small.

4.2 Mineral dust particles

We now investigate the AAC scene with mineral dust particles, referred as box (3) in Fig. 2a, which was observed on the 25 July 2008. The solutions obtained for various retrieval schemes are reported in Table 3. Solution 1* includes the retrieval of the fine and coarse mode particles load and size parameters and assumes a constant complex refractive index. Solution 2* includes in addition the retrieval of the imaginary part of the complex refractive index whereas solution 4 includes both the retrieval of the real and imaginary parts of the complex refractive index. For solution 4*, we made assumptions

AMTD
5, 6083–6145, 2012

for the coarse particles size parameter and for the real refractive index. The fraction of spherical particles (SF) is included in the retrieval scheme for all solutions and it is assumed the same in both modes.

The different solutions (1*, 2*, 3* and 4*) allows robust modelling the POLDER observations (e.g. see Fig. 8b for solution 4*). The algorithm retrieves AOT values larger than 1 and a large amount of non-spherical particles. The coarse mode effective radius retrieved for solutions 1*, 2* and 3* is too large and clearly not realistic for mineral dust particles. The standard deviation values for the coarse mode effective radius are also very large, which means that this parameter cannot be accurately retrieved. Again multiple solutions are possible and some assumptions must be considered. For solution 4*, the algorithm then retrieves a size distribution dominated by non-spherical coarse mode particles that shows much smaller absorption properties than biomass burning aerosols. Mineral dust particles also absorb the solar light due to the presence of iron oxide in their mineral composition (Derimian et al., 2008a). However, dust remains less absorbing than biomass burning aerosols, except probably for cases where it is mixed with carbonaceous material (Derimian et al., 2008b). Note that we should have retrieved the spectral dependence for the imaginary part of the complex refractive index since mineral dust particles typically show slightly higher absorption properties for shorter visible wavelengths (0.49 µm) than for larger wavelengths (0.67 and 0.865 µm). We however choose to hold constant this parameter with respect with wavelength to limit the number of retrieved parameters. This would have to be revised in case shorter wavelength observations would be incorporated.

We reported in Table 4 the results for the AAC scene with mineral dust particles observed on the 4 August 2008. The hyper-pixel is referred as box (4) in Fig. 3a and corresponds to case (3) in Table 4. We used solution 4* to analyze the data. The algorithm again retrieves the typical properties assumed for mineral dust particles. We observe that the contribution of the fine mode particles to the total AOT is much smaller (lower value of Angström exponent) than for the July case. Such variability in the size distribution of mineral dust particles is realistic according to Dubovik et al. (2002).

AMTD
5, 6083–6145, 2012

4.3 General comments on the refractive index retrieval

We generally retrieve a real refractive index lower than 1.47, when we include this parameter in the retrieval scheme for biomass burning aerosols but also for mineral dust particles. Dubovik et al. (2002) indicates an effective radius of about 0.13 µm (computed for an optical thickness of 0.9 at 0.44 µm) and real refractive index of 1.51, for biomass burning aerosols in the centre of South Africa. Our results indicate a larger effective radius (0.17 µm) and a smaller real refractive index (1.45 ± 0.015, see solution 4 in Table 3). The retrieved real part of the refractive index is also very low for mineral dust particles (1.41 ± 0.035). We noted that the decrease in the real refractive index in our retrievals is generally associated with an increase in the fine mode effective radius. This result suggests the AAC properties could be altered (an aged effect), which is likely to be possible since aerosols mix with wet air masses when they are transported over long distance in oceanic regions.

Knobelspiesse et al. (2011) found some difficulties in retrieving the real refractive index for AAC scenes with anthropogenic aerosols. They analyzed the off diagonal elements of the retrieval error covariance matrix and found large correlations between the errors associated with the retrieved particles real refractive index and size. We suggest that the retrieval of these two parameters is linked since they both largely affect the magnitude of the polarized phase function and affect it in an opposite way. Roughly, the P12 elements increase with the particles size increasing and the real refractive index decreasing. Polarized radiances measured over cloud-free ocean scenes show high sensitivity to the particles real refractive index for scattering angles larger than 130° (e.g. see Figs. 6 and 12 in Deuzé et al., 2000). We assume that some information about the aerosol microphysics is lost for AAC scenes by comparison with clear-sky ocean scenes, probably because the contribution of the cloud layer dominates the signal for scattering angles larger than 130°.

We also noted that the inclusion of the errors due to the 3-D cloud effects in the total error retrieval covariance matrix leads to the retrieval of weaker absorption properties

AMTD
5, 6083–6145, 2012

(smaller values for m_i) and therefore higher values of aerosol SSA. The retrieved values for the imaginary part of the complex refractive index are generally too times higher when the 3-D cloud effects are not accounted for.

4.4 Cloud droplets

The retrieved real refractive index values are in good agreement with what we expect for cloud droplets made of pure water (Hale et al., 1973). Our algorithm retrieves droplets effective radii varying between 8 and 12 µm with no peculiar geographical tendency. The retrieved droplets size distribution is much narrower (small values of effective variance) for the clouds observed southerneastern of the South Africa than for the clouds observed over the two other oceanic tropical regions located closer to Africa. This is good agreement with the results of Bréon and Doutriaux-Boucher (2005), who found that the droplets effective variance is generally much smaller for the clouds observed in subtropical and high-latitude oceans, than for continental regions and other oceanic regions. The reasons for this tendency cannot be currently established with confidence. We recall that the droplets effective variance was not much studied from space and that this parameter depends on the dynamical evolution of clouds (Politovich, 1993) and on the origin of the air mass (continental or maritime) (Martin et al., 2004).

Finally, we also compared the droplet effective radii retrieved with POLDER with those retrieved by MODIS. Table 5 show some comparisons performed for various scenes with aerosols above clouds and for the fields of clouds observed in pristine conditions. The droplet effective radius reported for MODIS is a mean value computed over the 200 km × 200 km area. Differences are expected between these two estimates since the polarized measurements are sensitive to droplets located at the top of the cloud layer whereas the MODIS total radiance measurements are sensitive to droplets located deeper in the cloud layer (Bréon and Doutriaux-Boucher, 2005). Another sources of differences are (1) that biases are expected on the MODIS retrieved droplets effective radius for AAC scenes with absorbing aerosols and (2) that the droplets effective variance is held constant in the MODIS algorithm (0.13). Bréon

AMTD
5, 6083–6145, 2012

and Doutriaux-Boucher (2005) found a systematic MODIS high bias of 2 µm in oceanic regions for droplets effective radii larger than 7 µm. The results obtained for the clouds observed in pristine conditions show a rather similar bias. The departures that we observed for AAC scenes are smaller than 2 µm, probably because the droplets effective radii retrieved by MODIS are underestimated due to the presence of absorbing AAC (Haywood et al., 2004).

5 Operational algorithm: the "single-pixel method"

5.1 Description

We use a look-Up-Table (L.U.T) approach to derive the aerosol properties above clouds using the observations acquired by POLDER at a fine spatial resolution. With respect with the so-called "hyper-pixel" method described in Sect. 3, we reduce the number of retrieved parameters to the AOT, the Angström exponent and the cloud droplets effective radius. The effects of the droplets effective radius and AOT are illustrated in Fig. 5. We calculate the polarized radiances using the SOS code for different combinations of aerosol and cloud particles models. We consider six fine mode aerosols models ($r_{g_f} = 0.06$, 0.08, 0.1, 0.12, 0.14, 0.16 µm and $\sigma_f = 0.4$) with a constant complex refractive index of 1.47–0.01i, which is a mean value for polluted and biomass burning aerosols. We also included the mineral dust particles model described in Table 3 (solution 4*). The elements of the polarized phase function were shown for similar particles models in previous studies (e.g. see Figs. 1 and 2 in Waquet et al., 2007). The polarized radiances are calculated for various AOTs and viewing geometries and interpolation processes are considered. For clouds particles, we consider 25 droplets models with effective radius varying between 5 and 26 µm by step of 1 µm, with a constant droplets variance of $v_{\text{eff\_cld}} = 0.06$ and a constant real refractive index ($m_{r\_\text{cld}}(0.490\,\mu\text{m}) = 1.338$, $m_{r\_\text{cld}}(0.670\,\mu\text{m}) = 1.331$ and $m_{r\_\text{cld}}(0.865\,\mu\text{m}) = 1.33$). We assume a cloud top height of 0.75 km and a value of 3.5 km for the aerosol layer

AMTD
5, 6083–6145, 2012

mean altitude. The effects of the atmospheric vertical profile on the measured polarized signal are small at 0.67 µm and almost negligible at 0.865 µm comparing to 0.49 µm and we therefore restrict our algorithm to these two bands. A schematic view of the algorithm is shown in Fig. 9.

A different retrieval strategy is considered depending on the aerosol type and load. We first estimate the AOT above clouds by using all the angular available information and by only considering the six fine mode particles models. If the retrieved AOT is larger than 0.1 at 0.865 µm, we then compare the least square error term computed for the mineral dust particles model with ones computed for the six other fine mode particles models and keep the solution obtained with the mineral dust model if this latter model minimizes the error term. The threshold of 0.1 in AOT is justified because the retrieval of the dust AOT becomes difficult (instable) when the AAC optical thickness becomes small. This is probably due to the 3-D clouds effects that make difficult the modelling of the primary cloud-bow when the atmosphere above clouds is pristine, as shown in Sect. 4. If the AOT retrieved at the first step is smaller than 0.1 or if the mineral dust particles model fails to reproduce data, we then restrict the algorithm to observations acquired at scattering angles smaller than 130° and only consider the six fine mode particles models. The inclusion of the data acquired in the polarized cloud bow is not critical for the retrieval of fine mode particles properties, at least when a limited number of parameters is considered. The retrieval strategy also incorporates the fact that the POLDER instrument sometimes does not observe the side scattering and forward scattering geometries (data for $\Theta < 130°$ unavailable).

Different filters are eventually applied to the data to obtain a quality assessed product. We only keep homogenous cloudy pixels associated with optically thick clouds ($\Delta\_COD < 5$ and $\Delta\_REFF\_CLD < 5$ and $COD > 5$). We added a criterion that allows rejecting pixels for which the POLDER data are not accurately fitted ($\varepsilon < 0.005$). We only consider thermodynamic cloud phase index values ranging between 0 and 80 (only liquid clouds) and between 81 and 120 ("mixed-phase clouds") since AAC scenes are sometimes improperly classified as "mixed-phase clouds". We added another criterion

AMTD
5, 6083–6145, 2012

to reject multi-layer scenes with cirrus above liquid clouds. This latter criterion is based on the cloud top pressure anomalies observed for scenes with cirrus above liquid clouds ($z_c\_O_2 < z_c\_\text{Rayleigh} < z_c\_\text{IR}$, see Fig. 2 in Waquet et al., 2009a). This latter criterion is only applied when all these three estimates of the cloud top pressure provided by POLDER and MODIS are available and when the anomaly is strong ($z_c\_\text{IR} - z_c\_O_2 > 2\,\text{km}$ and $z_c\_\text{IR} - z_c\_\text{Rayleigh} > 2\,\text{km}$). The AOT is finally aggregated at a spatial resolution of $18 \times 18\,\text{km}^2$ and we only keep these pixels for which the AOT standard deviation (Δ_AOT) is smaller than 0.1 and contain more than four $6 \times 6\,\text{km}^2$ pixels. This latter description allows rejecting the edges of the clouds where our retrieved AOT are generally doubtful and where the radiances should be not modelled with a plane parallel transfer radiative code.

5.2 Effects of various approximations

The polarized radiances included in the LUT are calculated using a truncated phase function since the errors induced by this approximation are small. The droplet effective radius can be derived as a part of the retrieval process or estimated using the one retrieved by MODIS. We compare both approaches and found only small differences in the retrieved AAC optical thickness. We then choose to use the MODIS droplets effective radius since its retrieval does not depend on the availability of a particular viewing geometry. The effects of this approximation on the retrieved AOT for dust particles are evaluated using synthetic data. We simulated polarized radiances for AAC scenes with mineral dust particles. We considered the mineral dust particles model given in Table 3 for solution 4* and an AOT of 1.05 at 0.865 µm. The mineral dust layer is above a liquid water cloud with a droplet effective radius of 10.5 µm, an effective variance of 0.09 and an optical thickness of 5. We considered 16 viewing geometries with scattering angles ranging between 80° and 160°. Note that the selected cloud microphysical parameters and viewing geometries are not included in the LUT. The algorithm retrieves the dust model and an AOT that is very close to the input AOT (1.04 at 0.865 µm). This confirms that the different interpolations considered for the modelling of the polarized radiance

AMTD
5, 6083–6145, 2012

only weakly affect the retrieval of the AOT. We perturbed the retrieval by increasing and decreasing the droplets effective radius, respectively by 2 µm and found a maximal error of 0.03 in the AOT. We decreased by 14 % the magnitude of the synthetic polarized radiances in the cloud-bow directions to evaluate the impacts on the AOT due to the uncertainties in modelling the primary cloud-bow magnitude (due to 3-D cloud effects and truncation effects). We found that the algorithm then overestimates the true AOT by 12.5 %. The error reaches 14 % if we also perturb the cloud droplet effective radius by 2 µm at the same time. We also note that the errors slightly increase when a small value of cloud droplet variance is considered in the input simulation (e.g. 0.03 instead of 0.09). Note that these different sources of errors only weakly affect the retrieval of fine mode particles properties, for which we only consider data acquired for scattering angles smaller than 130°. Note also that this analysis does not account for potential errors due to the assumptions made for the aerosol microphysical properties.

5.3 First results

5.3.1 Case studies

The spatial variability of the AOT of the dust plume transported above clouds on the 25 August 2008 is shown in Fig. 10a, together with the AOT retrieved over cloud-free ocean. This is a combination of AOT retrieved with the operational algorithm for cloud-free scenes (Herman et al., 2005) and with method previously described for cloudy scenes. The AOT map shows that the dust plume is blowing east over the ocean and then southeast above low-level clouds. The AAC algorithm retrieves the dust model included in the LUT and the retrieved Angström exponent is therefore about 0.4. Figure 10a shows a good qualitative spatial agreement between the AOTs retrieved over cloudy and cloud-free pixels. We however note that the AAC optical thicknesses are systematically smaller than the ones retrieved over clear-sky ocean pixels. For instance, the maximal AOT retrieved above clouds and cloud-free ocean are, respectively equal to 1.5 and 1.7. Such a difference is not surprising since the AAC optical thickness

AMTD
5, 6083–6145, 2012

does not include the aerosols located in the lower atmosphere layer that were detected over cloud-free scenes by CALIOP. The results obtained for the mineral dust particles observed on the 4 August 2008 are reported in Fig. 10b. The same observations can be made for this second case study. The fact that the algorithm does not retrieved AOT over clouds that are larger than the total column AOT is also a positive sign of the retrieval consistency.

For the case study on the biomass burning aerosols, we compare the AAC optical thickness with the fine mode AOT retrieved by POLDER over cloud-free pixels. We assume that most of the fine mode particles are located in the elevated biomass burning aerosols layer. Therefore, the fine mode AOT retrieved above cloud-free pixels with the ocean algorithm and the AAC optical thickness retrieved with anthropogenic particles models should be rather comparable. Figure 11b shows a general good qualitative spatial agreement between the AOTs retrieved over both type of scenes. The largest AAC optical thicknesses (> 0.3) are retrieved over the Gulf of Guinea and are associated with small particles (α of ≈ 2.25). In this region, the AAC optical thicknesses are higher than the AOTs retrieved for ocean scenes. In this region, the spatial variability of the fine mode AOT retrieved over clear-sky ocean pixels is sometimes questionable. For instance, the fine mode AOT abruptly changes from about 0.16 to 0.24 (from blue to yellow in the AOT map shown in Fig. 11a) around the point of coordinates longitude 4° and latitude −9°. The change in the fine mode AOT is associated with a change on the coarse mode microphysical properties (the fraction of non-spherical particles changed). Biomass burning aerosols are very likely to be strong absorbing particles. We think that the assumption of non-absorbing particles made in the ocean algorithm might lead this method to slightly overestimate the coarse mode AOT and then to consequently underestimate the scattering fine mode AOT. This hypothesis is supported by the results of the sensitivity analysis presented in this work showed that the assumption of a weak absorption generally leads to the retrieval of a larger coarse mode AOT (see solutions 2 and 4 in Table 2).

AMTD
5, 6083–6145, 2012

5.3.2 Mean results

We reported the AOT retrieved at 0.865 µm above clouds with the previous method for four different regions of the Earth in Fig. 12. We report average values computed over a period of three months. The investigated time period is from 1 June to 31 August 2008. We considered four large grid square areas that mainly include ocean cloudy scenes. Two areas are centered on the regions previously introduced in Sect. 3. We selected two other regions respectively located in the northeastern and southeastern parts of the Pacific Ocean where low-level cloud decks are typically present.

The largest AOTs are retrieved over the tropical North East Atlantic region close to Sahara. The algorithm detects mineral dust particles. The AOT varies between 0.3 and 0.8 and reaches maximal values near the African coasts and the mean Angström exponent is about 0.4. The scale color was not stretched to make more visible the aerosols structures observed near California. Other average large AOT values (> 0.2) are retrieved for the tropical southeast Atlantic region near the regions of vegetation fires in South Africa. Figure 13 shows a zoom for the mean Angström exponent retrieved above clouds for this region. The algorithm retrieves small particles models. We observe a decrease in the Angström exponent as we progressively move away from South Africa. The mean Angström exponent progressively decreases from 2.4 to 1.7, from the east to the west, which corresponds to an increase of 0.06 µm for the effective radius in our aerosol model database.

Low-level clouds typically cover the region of the Pacific Ocean that boards the South America coasts along Peru and Chile. According to our results, this region does not show significant occurrence of aerosols above clouds. The presence of biomass burning aerosols is expected in South America in August but the Andes Mountain certainly prevents anthropogenic aerosols to be transported over this part of the Pacific Ocean, at least for the considered time period. A significant aerosol above cloud signal (AOT of about 0.1) is observed over the Pacific Ocean near the Californian coasts. Several vegetation fires occurred in California during the summer 2008 due to an exceptional

AMTD
5, 6083–6145, 2012

dry spring and the transport of biomass burning aerosols above clouds is very likely, although regional circulation does not usually transport aerosols westwards. The algorithm retrieves a mean small Angström exponent (≈ 2.1), which confirms the presence of fine mode particles.

6 Conclusions

This study confirms that passive sensors with angular, spectral and polarized capabilities have a strong potential for retrieving the Aerosols Above Clouds (AAC) optical and microphysical properties. We developed two different algorithms to analyze the POLDER data for AAC scenes. The first one, the so-called the "hyper-pixel" method, allows a simultaneous retrieval of the aerosol and cloud properties and uses POLDER data aggregated at a coarse resolution. The method retrieves the mean properties of the observed particles under the assumption of spatial homogeneity. The sensitivity analysis presented in this work showed that polarization measurements provided by POLDER do not contain enough information to fully constrains all the AAC properties. For aerosols, the method is primarily sensitive to the aerosol optical thickness, size distribution, shape and real refractive index. The retrieval of the complex refractive index however remains difficult. Our results suggest that the size and the real refractive index of fine mode aerosols could be respectively larger and smaller when the particles are observed above clouds, in oceanic regions, than when these particles are observed over land near the sources. We make clear that this method cannot be used to retrieve the aerosol SSA since the method failed to accurately separate the absorption optical thickness and the coarse mode optical thickness for AAC scenes with biomass burning aerosols.

The aerosols layer attenuates the magnitudes of the primary and surnumerary cloud bows generated by the underlying liquid cloud layer. This effect must be corrected (or included in the retrieval process) if an accurate estimate of the cloud droplets microphysical properties has to be achieved for AAC retrievals from polarization

AMTD
5, 6083–6145, 2012

measurements. Our results confirm that the droplets size distribution is narrow in high latitude ocean regions and that the droplets effective radius retrieved from polarization measurements is generally slightly smaller than the one retrieved by passive sensors that uses total radiance measurements, such as the MODIS instrument (departures smaller than 2 µm). We found that the magnitude of the primary cloud bow cannot be accurately estimated with a plane parallel transfer radiative code. Using a 3-D radiative transfer code, we shown that the values are reduced in the cloud-bow. The errors for the modelling of the polarized radiances vary between 5 and 8 %, for the case done, depending on wavelength and viewing geometry. The use of this method for a global treatment could certainly benefit for both the aerosol and cloud studies. This method is however currently too time consuming and requires an aggregation of the data that is not always possible. We plan to use this method for further case studies analysis.

A less sophisticated algorithm was developed to retrieve the AOT and the Angström exponent for AAC scenes at a fine spatial resolution in a more operational processing. With respect with the algorithm described in Waquet et al. (2009a), we improved the accuracy of the modelling, included a realistic mode for mineral dust particles and developed a retrieval strategy that takes advantage of the measurements acquired in the cloud-bow direction. The method is however limited to observations acquired for optically thick clouds (optical thickness > 5) and only considers a finite number of aerosol models. An interesting result of this study is that polarized measurements acquired in the cloud-bow can be used to retrieve the optical thickness of the mineral dust particles residing above liquid clouds. These large non-spherical particles do not much polarize light but strongly attenuate the polarized cloud bow generated by the beneath liquid cloud layer. The spectral attenuation can be used to qualitatively identify the nature of the particles (coarse or fine mode particles) whereas the magnitude of the attenuation is related to the optical thickness of the aerosol layer. We compared the AOTs retrieved above clouds with ones retrieved closely over clear-sky ocean pixels. We found maximal differences of 0.2 in AOT at 0.865 µm that can be explained either by the assumptions used for the microphysical properties of the aerosols, that are different

AMTD
5, 6083–6145, 2012

in the two algorithms, or because the algorithm developed for cloud-free ocean scenes measures the aerosol load integrated over the entire atmospheric column whereas the AAC algorithm only retrieves the AOT of the particles residing above the cloud top.

More efforts are needed to better characterize the aerosols above clouds properties. The AOT retrieved with the lidar CALIOP could be considered in future efforts to check the coherence of our retrievals made over clouds or to better constrain the retrieval of the aerosol microphysics using innovative synergetic approaches. Other POLDER data could be also potentially included in the method, such as the total radiance measurements. We however point out that the present algorithm, solely based on the use of polarization measurements, has the high advantage, with respect with other passive methods, of being independent on the albedo of the cloud layer.

When a high loading of strong absorbing aerosols is present above clouds, a rather strong positive radiative forcing is expected as well as significant biases on the retrieved cloud properties. The first results obtained with POLDER indicate large mean AOTs above clouds for oceanic regions near the coasts of South Africa and California that correspond to biomass burning aerosols whereas even larger mean AOTs above clouds are retrieved near the coasts of Senegal (for June–August 2008). More investigations are therefore needed to better describe the spatial and temporal variability of the AAC properties. Our next step is to analyze the complete archive of POLDER data for AAC scenes. This would provide a first global estimate of the properties of the aerosols suspended above clouds and so to first estimate the much uncertain aerosol direct forcing over cloudy skies.

Appendix A

The retrieval error covariance matrix for the optical thickness τ.

$$\mathbf{C}_\tau = \mathbf{K}_\tau \mathbf{C}_X \mathbf{K}_\tau^T \quad \text{(A1)}$$

AMTD
5, 6083–6145, 2012

where $\mathbf{K}_\tau$ is the Jacobian matrix for τ. The same formula stands for the aerosol single scattering albedo (ϖ_0) and effective radius (r_{eff}).

The effective radius, r_{eff}, for log normal size distribution is defined as:

$$r_{\text{eff}} = r_g \exp\left(\frac{5}{2}\sigma^2\right) \tag{A2}$$

Mean squared error term ε calculated between the measured and calculated polarized radiances:

$$\varepsilon = \sqrt{\frac{1}{N_\Theta N_\lambda} \sum_{i=1}^{N_\Theta} \sum_{j=1}^{N_\lambda} \left[L_{ij}^{\text{mes}}(\Theta) - L_{ij}^{\text{calc}}(\Theta)\right]^2} \tag{A3}$$

where N_λ and N_Θ are, respectively the number of selected viewing directions and the number of channels.

References

Ackerman, A. S., Toon, O. B., Stevens, D. E., Heymsfeld, A. J., Ramanathan V., and Welton. E. J.: Reduction of tropical cloudiness by soot, Science, 288, 1042–1047, doi:10.1126/science.288.5468.1042, 2000.

Ackermann, J.: The extinction-to-backscatter ratio of tropospheric aerosol: a numerical study, J. Atmos. Ocean. Tech., 15, 1043–1050, 1998.

Bréon, F.-M. and Doutriaux-Boucher, M.: A comparison of cloud droplet radii measured from space, IEEE T. Geosci. Remote, 43, 1796–1805, 2005.

Bréon, F.-M. and Goloub, P.: Cloud droplet effective radius from spaceborne polarization measurements, Geophys. Res. Lett., 25, 1879–1882, 1998.

Bréon, F.-M., Tanré, D., and Generoso, S.: Aerosol effect on cloud droplet size monitored from satellite, Science, 295, 834–838, 2002.

AMTD
5, 6083–6145, 2012

Cattrall, C., Reagan, J., Thome, J. K., and Dubovik, O.: Variability of aerosol and spectral lidar and backscatter and extinction ratios of key aerosol types derived from selected aerosol robotic network locations, J. Geophys. Res., 110, D10S11, doi:10.1029/2004JD005124, 2005.

Chand, D., Wood, R., Anderson, T. L., Satheesh, S. K., and Charlson, R. J.: Satellite-derived direct radiative effect of aerosols dependent on cloud cover, Nat. Geosci., 2, 181–184, 2009.

Chen, B., Huang, J., Minnis, P., Hu, Y., Yi, Y., Liu, Z., Zhang, D., and Wang, X.: Detection of dust aerosol by combining CALIPSO active lidar and passive IIR measurements, Atmos. Chem. Phys., 10, 4241–4251, doi:10.5194/acp-10-4241-2010, 2010.

Coddington, O. M., Pilewskie, P., Redemann, J., Platnick, S., Russell, P. B., Schmidt, K. S., Gore, W. J., Livingston, J., Wind G., and Vukicevic, T.: Examining the impact of overlying aerosols on the retrieval of cloud optical properties from passive remote sensing, J. Geophys. Res., 115, D10211, doi:10.1029/2009JD012829, 2010.

Cornet, C., Labonnote L. C., and Szczap, F.: Three-dimensional Polarized Monte-Carlo Atmospheric Radiative Transfer Model (3DMCPOL): 3-D effects on polarized visible reflectances of a cirrus cloud, J. Quant. Spectrosc. Rad. Transfer, 111, 174–186, doi:10.1016/j.jqsrt.2009.06.013, 2010.

De Graaf, M., Stammes P., and Aben, E. A. A.: Analysis of reflectance spectra of UV-absorbing aerosol scenes measured by SCIAMACHY, J. Geophys. Res., 112, D02206, doi:10.1029/2006JD007249, 2007.

Derimian, Y., Karnieli, A., Kaufman, Y. J., Andreae, M. O., Andreae, T. W., Dubovik, O., Maenhaut, W., and Koren, I.: The role of iron and black carbon in aerosol light absorption, Atmos. Chem. Phys., 8, 3623–3637, doi:10.5194/acp-8-3623-2008, 2008a.

Derimian, Y., Léon, J.-F., Dubovik, O., Chiapello, I., Tanré, D., Sinyuk, A., Auriol, F., Podvin, T., Brogniez, G., and Holben, B. N.: Radiative properties of aerosol mixture observed during the dry season 2006 over M'Bour, Senegal (African monsoon multidisciplinary analysis campaign), J. Geophys. Res., 113, D00C09, doi:10.1029/2008JD009904, 2008b.

Deuzé J.-L., Goloub, P., Herman, M., Marchand, A., Perry, G., Tanré, D., and Susana, S.: Estimate of the aerosols properties over the ocean with POLDER, J. Geophys Res, 105, 15329–15346, 2000.

Dubovik, O., Holben, B. N., Eck, F. T., Smirnov, A., Kaufman, J. Y., King, D. M., Tanré, D., and Slutsker, I.: Variability of absorption and optical properties of key aerosol types observed in worldwide locations, J. Atmos. Sci., 59, 590–608, 2002.

AMTD
5, 6083–6145, 2012

Dubovik, O., Sinyuk, A., Lapyonok, T., Holben, B. N., Mishchenko, M., Yang, P., Eck, T. F., Volten, H., Muñoz, O., Veihelmann, B., van der Zande, W. J., Leon, J.-F., Sorokin, M., and Slutsker, I.: Application of spheroid models to account for aerosol particle nonsphericity in remote sensing of desert dust, J. Geophys. Res., 111, D11208, doi:10.1029/2005JD006619, 2006.

Eck, T. F., Holben, B. N., Ward, D. E., Mukelabai, M. M., Dubovik, O., Smirnov, A., Schafer, J. S., Hsu, N. C., Piketh, S. J., Queface, A., Le Roux, J., Swap, R. J., and Slutsker, I.: Variability of biomass burning aerosol optical characteristics in southern Africa during the SAFARI 2000 dry season campaign and a comparison of single scattering albedo estimates from radiometric measurements, J. Geophys. Res., 108, 8477–8493, doi:10.1029/2002JD002321, 2003.

Ferlay, N., Thieuleux, F., Cornet, C., Davis, A. B., Dubuisson, P., Ducos, F., Parol, F., Riédi, J., and Vanbauce, C.: Toward new inferences about cloud structures from multidirectional measurements in the oxygen A band: Middle-of-cloud pressure and cloud geometrical thickness from POLDER3/PARASOL, J. Appl. Meteorol. Clim, 49, 2492–2507, doi:10.1175/2010JAMC2550.1, 2010.

Forster, P., Ramaswamy, V., Artaxo, P., Berntsen, T., Betts, R., Fahey, D. W., Haywood, J., Lean, J., Lowe, D. C., Myhre, G., Nganga, J., Prinn, R., Raga, G., Schulz, M., and Van Dorland, R.: Changes in Atmospheric Constituents and in Radiative Forcing, in Climate Change 2007: The Physical Science Basis. Contribution of Working Group I to the Fourth Assessment Report of the Intergovernmental Panel on Climate Change, edited by: Solomon, S., Qin, D., Manning, M., Chen, Z., Marquis, M., Averyt, K. B., Tignor, M., and Miller, H. L., Cambridge University Press, Cambridge, UK and New York, NY, USA, 129–234, 2007.

Fougnie, B., Bracco, G., Lafrance, B., Ruffel, C., Hagolle, O., and Tinel, C.: PARASOL in-flight calibration and performance, Appl. Opt., 46, 5435–5451, 2007.

Goloub, P., Deuzé J.-L., Herman, M., and Fouquart, Y.: Analysis of the POLDER polarization measurements performed over cloud covers, IEEE T. Geosci. Remote, 32, 78–88, 1994.

Hale, G. M. and Querry, M. R.: Optical constants of water in the 200-nm to 200-µm wavelength region, Appl. Opt., 12, 555–563, 1973.

Hansen, J. E. and Travis, L. D.: Light scattering in planetary atmospheres, Space Sci. Rev., 16, 527–610, doi:10.1007/BF00168069, 1974.

Hasekamp, O. P.: Capability of multi-viewing-angle photo-polarimetric measurements for the simultaneous retrieval of aerosol and cloud properties, Atmos. Meas. Tech., 3, 839–851, doi:10.5194/amt-3-839-2010, 2010.

AMTD
5, 6083–6145, 2012

Haywood, J. M. and Boucher, O.: Estimates of the direct and indirect radiative forcing due to tropospheric aerosols: a review., Revs. Geophys., 38, 513–543, 2000.
Haywood, J. M., Osborne, S. R., Francis, P., Glew, M., Highwood, E., Formenti, P., and Andreae, M.: Radiative properties and direct radiative effect of Saharan dust measured by the C-130 aircraft during SHADE: 1. Solar spectrum, J. Geophys. Res., 108, 8577–8592, doi:10.1029/2002JD002687, 2003a.
Haywood, J. M., Osborne, S. R., Francis, P. N., Keil, A., Formenti, P., Andreae, O. M., and Kaye, P. H.: The mean physical and optical properties of regional haze dominated by biomass burning aerosol measured from the C-130 aircraft during SAFARI 2000, J. Geophys. Res., 108, 8473–8486, 2003b.
Haywood, J. M., Osborne, S. R., and Abel, S. J.: The effect of overlying absorbing aerosol layers on remote sensing retrievals of cloud effective radius and cloud optical depth, Q. J. Roy. Meteorol. Soc., 130, 779–800, 2004.
Herman, M., Deuzé, J.-L., Marchand, A., Roger, B., and Lallart, P.: Aerosol remote sensing from POLDER/ADEOS over the ocean: improved retrieval using a nonspherical particle model, J. Geophys. Res., 110, D10S02, doi:10.1029/2004JD004798, 2005.
Hsu, N. C., Herman, J. R., and Chen, S.-C.: Radiative impacts from biomass burning in the presence of clouds during boreal spring in southeast Asia, Geophys. Res. Lett., 30, 1224–1227, doi:10.1029/2002GL016485, 2003.
Hu, Y., Vaughan, M., Liu, Z., Powell, K., and Rodier., S.: Retrieving optical depths and lidar ratios for transparent layers above opaque water clouds from calipso lidar measurements, IEEE Geosci. Remote Sens. Lett., 4, 523–526, 2007.
Johnson, B. T., Shine, K. P., and Forster, P. M.: The semi-direct aerosol effect: impact of absorbing aerosols on marine stratocumulus, Q. J. R. Meteorol. Soc., 130, 1407–1422, doi:10.1256/qj.03.61, 2004.
Kaufman, Y., Tanré, D., and Boucher, O.: A satellite view of aerosols in the climate system, Nature, 419, 215–223, 2002.
Kalashnikova, O. V., Kahn, R., Sokolik, I. N., and Li, W.-H.: Ability of multiangle remote sensing observations to identify and distinguish mineral dust types: optical models and retrievals of optically thick plumes, J. Geophys. Res., 110, D18S14, doi:10.1029/2004JD004550, 2005.
Keil, A. and Haywood, J. M.: Solar radiative forcing by biomass burning aerosol particles during SAFARI 2000: A case study based on measured aerosol and cloud properties, J. Geophys. Res., 108, 8467–8476, 2003.

AMTD
5, 6083–6145, 2012

Knobelspiesse, K., Cairns, B., Redemann, J., Bergstrom, R. W., and Stohl, A.: Simultaneous retrieval of aerosol and cloud properties during the MILAGRO field campaign, Atmos. Chem. Phys., 11, 6245–6263, doi:10.5194/acp-11-6245-2011, 2011.

Leahy, L. V., Anderson, T. L., Eck, T. F., and Bergstrom, R. W.: A synthesis of single scattering albedo of biomass burning aerosol over Southern Africa during SAFARI 2000, Geophys. Res. Lett., 34, L12814, 2007.

Lenoble, J., Herman, M., Deuzé, J. L., Lafrance, B., Santer, R., and Tanré, D.: A successive order of scattering code for solving the vector equation of transfer in the earths atmosphere with aerosols Journal of Quantitative Spectroscopy and Radiative Transfer, 107, 479–507, doi:10.1016/j.jqsrt.2007.03.010, 2007.

Martin, G. M., Johnson, D. W., and Spice, A.: The measurement and parameterization of effective radius of droplets in warm stratocumulus clouds, J. Atmos. Sci., 51, 1823–1842, 1994.

Marshak, A. and Davis, A. B.: 3-D Radiative Transfer in Cloudy Atmospheres, Springer, New York, p. 686, 2005.

Menzel, W. P., Frey, R. A., Baum, B. A., and Zhang, H.: Cloud-top properties and cloud phase algorithm theoretical basis document, version 7, available online at: http://modisatmos.gsfc.nasa.gov/_docs/MOD06CT:MYD06CT_ATBD_C005.pdf, last access: August 2012, 55 pp., 2006.

Mishchenko, M. I. and Travis, L. D.: T-matrix computations of light scattering by large spheroidal particles, Opt. Commun., 109, 16–21, 1994.

Mishchenko, M. I. and Travis, L. D.: Satellite retrieval of aerosol properties over the ocean using polarization as well as intensity of reflected sunlight, J. Geophys. Res. 102, 16989–17013, 1997.

Mishchenko, M., Cairns, B., Kopp, G., Schueler, C., Fafaul, B., Hansen, J., Hooker, R., Itchkawich, T., Maring, H., and Travis, L.: Accurate monitoring of terrestrial aerosols and total solar irradiance: introducing the Glory mission, B. Am. Meteorol. Soc, 88, 677–691, 2007.

Nakajima, T. and Tanaka, M.: Algorithms for radiative intensity calculations in moderately thick atmospheres using a truncation approximation, J. Quant. Spectrosc. Ra., 40, 51–69, 1988.

Parol, F., Buriez, J. C., Vanbauce, C., Riedi, J., Labonnote, L. C., Doutriaux-Boucher, M., Vesperini, M., Sèze, G., Couvert, P., Viollier, M., and Bréon F. M.: Capabilities of multi-angle polarization cloud measurements from satellite: POLDER results, Adv. Space Res., 33, 1080–1088, 2004.

AMTD
5, 6083–6145, 2012

Peters, K., Quaas, J., and Bellouin, N.: Effects of absorbing aerosols in cloudy skies: a satellite study over the Atlantic Ocean, Atmos. Chem. Phys., 11, 1393–1404, doi:10.5194/acp-11-1393-2011, 2011.

Platnik, S., King, M. D., Ackerman, S. A., Menzel, W. P., Baum, B. A., Riédi, J. C., and Frey, R. A.: The MODIS Cloud Products: algorithms and examples from Terra, IEEE T. Geosci. Remote, 41, 459–473, 2003.

Politovich, M. K.: A study of the broadening of droplet size distributions in cumuli, J. Atmos. Sci., 50, 2230–2244, 1993.

Potter, J.:The delta function approximation in radiative transfer theory, J. Atmos. Sci., 27, 943–949, 1970.

Ramanathan, V., Crutzen, P. J., Lelieveld, J., Mitra, A. P., Althausen, D., Anderson, J., Andreae, M. O., Cantrell, W., Cass, G. R., Chung, C. E., Clarke, A. D., Coakley, J. A., Collins, W. D., Conant, W. C., Dulac, F., Heintzenberg, J., Heymsfield, A. J., Holben, B., Howell, S., Hudson, J., Jayaraman, A., Kiehl, J. T., Krishnamurti, T. N., Lubin, D., McFarquhar, G., Novakov, T., Ogren, J. A., Podgorny, I. A., Prather, K., Priestley, K., Prospero, J. M., Quinn, P. K., Rajeev, K., Rasch, P., Rupert, S., Sadourny, R., Satheesh, S. K., Shaw, G. E., Sheridan, P., and Valero, F. P. J.: The Indian Ocean Experiment: An Integrated Assessment of the Climate Forcing and Effects of the Great Indo-Asian haze, J. Geophys. Res., 106, 28371–28393, 2001.

Riedi, J., Marchant, B., Platnick, S., Baum, B. A., Thieuleux, F., Oudard, C., Parol, F., Nicolas, J.-M., and Dubuisson, P.: Cloud thermodynamic phase inferred from merged POLDER and MODIS data, Atmos. Chem. Phys., 10, 11851–11865, doi:10.5194/acp-10-11851-2010, 2010.

Rodgers, C. D.: Inverse methods for atmospheric sounding: theory and practice, World Scientific Publishing Co. Ltd, London, UK, p. 238, 2000.

Rosenfeld, D.: Suppression of rain and snow by urban and industrial air pollution, Science, 287, 1793–1796, 2000.

Salomonson, V. V., Barnes, W. L., Maymon, P. W., Montgomery, H. E., and Ostrow, H.: MODIS: advanced facility instrument for studies of the Earth as a system, IEEE T. Geosci. Remote, 27, 145–153, 1989.

Tanré, D., Bréon, F.-M., Deuzé, J.-L., Herman, M., Goloub, P., Nadal, F., and Marchand, A.: Global observation of anthropogenic aerosols from satellite, Geophys. Res. Lett., 28, 24, 4555–4558, 2001.

AMTD
5, 6083–6145, 2012

Torres, O., Jethva, H., and Bhartia, P. K.: Retrieval of aerosol optical depth above clouds from OMI observations: sensitivity analysis and case studies, J. Atmos. Sci., 69, 1037–1053. doi:10.1175/JAS-D-11-0130.1, 2012.

Twomey, S.: The influence of pollution on the shortwave albedo of clouds, J. Atmos. Sci., 34, 1149–1152, 1977.

Vanbauce, C., Cadet, B., and Marchand, R. T.: Comparison of POLDER apparent and corrected oxygen pressure to ARM/MMCR cloud boundary pressures, Geophys. Res. Lett., 30, 1212–1215, doi:10.1029/2002GL016449, 2003.

Vaughan, M., Young, S., Winker, D., Powell, K., Omar, A., Liu, Z., Hu, Y., and Hostetler C.: Fully automated analysis of space-based lidar data: an overview of the CALIPSO retrieval algorithms and data products, in: Laser Radar Techniques for Atmospheric Sensing, edited by: Singh, U. N., International Society for Optical Engineering (SPIE Proceedings, Vol. 5575), 16–30, doi:10.1117/12.572024, 2004.

Volten, H., Munõz, O., Rol, E., de Haan, J. F., Vassen, W., Hovenier, J. W., Muinonen, K., and Nousiainen, T.: Scattering matrices of mineral aerosol particles at 441.6 nm and 632.8 nm, J. Geophys. Res., 106, 17375–17401, 2001.

Waquet, F., Goloub, P., Deuzé, J.-L., Léon, J.-F., Auriol, F., Verwaerde, C., Balois, J.-Y., and François, P.: Aerosol retrieval over land using a multiband polarimeter and comparison with path radiance method, J. Geophys. Res., 112, D11214, doi:10.1029/2006JD008029, 2007.

Waquet, F., Riedi, J., Labonnote, L. C., Goloub, P., Cairns, B., Deuzé, J.-L., and Tanré, D.: Aerosol remote sensing over clouds using the A-Train observations, Journal of Atmospheric Sciences, 66, 2468–2480, doi:10.1175/2009JAS3026.1, 2009a.

Waquet, F., Cairns, B., Knobelspiesse, K., Chowdhary, J., Travis, L. D., Schmid, B., and Mishchenko, M. I.: Polarimetric remote sensing of aerosols over land, J. Geophys. Res., 114, D01206–D01228, doi:10.1029/2008JD010619, 2009b.

Wilcox, E. M.: Direct and semi-direct radiative forcing of smoke aerosols over clouds, Atmos. Chem. Phys., 12, 139–149, doi:10.5194/acp-12-139-2012, 2012.

Winker, D. M., Hunt, W. H., and Hostetler, C. A.: Status and performance of the CALIOP lidar, in: Laser Radar Techniques for Atmospheric Sensing, edited by: Singh, U. N., International Society for Optical Engineering (SPIE Proceedings, Vol. 5575), 8–15, doi:10.1117/12.571955, 2004.

AMTD
5, 6083–6145, 2012

Table 1. A priori knowledge of the aerosol and cloud parameters and associated uncertainties ().

Parameters	τ_{-f}	τ_{-c}	r_{g-f} (µm) σ_{-f}	r_{g-c} (µm) σ_{-c}	m_r	m_i	Shape (SF)	r_{eff_cld} (µm)	v_{eff_cld}	m_{r-cld} 0.49 µm 0.67 µm 0.865 µm
A priori information	5.10^{-3} (+∞)	10^{-3} (+∞)	0.15 (0.1) 0.4 (0.2)	0.8 (0.1) 0.6 (0.3)	1.47 (0.14)	10^{-3} (0.1)	0.5 (0.5)	10.0 (10.0)	0.06 (0.06)	1.338 (0.01) 1.331 (0.01) 1.330 (0.01)

AMTD
5, 6083–6145, 2012

Table 2. Aerosol and cloud retrieved parameters for various inversion schemes in case of a biomass burning particles layer located above a liquid cloud and associated uncertainties The cloudy area is shown in Fig. 1a (box 1). The different solutions correspond to the adjustement of a different number of parameters. The parameters that are not adjusted during the retrieval process are indicated in bold. ε is the mean squared error term calculated between the measured and simulated polarized radiances ($\times 10^3$).

$\tau(\lambda)$ 865 nm –> 490 nm	α	$r_{\text{eff,f}}$ (µm)	$r_{\text{eff,c}}$ (µm)	m_i	$\omega_0(\lambda)$ 865 nm –> 490 nm	m_r	Shape (SF)	$r_{\text{eff\_cld}}$ (µm) $v_{\text{eff\_cld}}$ $m_{r\text{-cld}}(\lambda)$ 865 nm –> 490 nm	ε $\times 10^3$
Solution 1									
0.25(0.01) 0.46(0.01) 0.82(0.015)	2.32 (0.20)	0.175 (0.001)	No coarse mode particles	**0.001**	0.992(10^{-4}) 0.9935(10^{-4}) 0.9945(10^{-4})	**1.47**	**1**	8.3(0.3) 0.10(0.01) 1.330(0.001) 1.333(0.003) 1.344(0.003)	1.229
Solution 2									
0.29(0.015) 0.48(0.02) 0.84(0.02)	2.0 (0.35)	0.171 (0.0015)	1.74 (0.12)	**0.001**	0.988(10^{-4}) 0.9902(10^{-4}) 0.992(10^{-4})	**1.47**	**1**	8.3(0.3) 0.09(0.015) 1.330(0.002) 1.334(0.003) 1.345(0.003)	1.137
Solution 3									
0.31(0.02) 0.51(0.02) 0.87(0.025)	1.90 (0.36)	0.165 (0.002)	2.77 (0.43)	0.014 (.0035)	0.84(0.035) 0.875(0.03) 0.90(0.025)	**1.47**	**1**	8.4(0.3) 0.08(0.015) 1.331(0.002) 1.334(0.003) 1.344(0.003)	1.051
Solution 4									
0.30(0.025) 0.50(0.02) 0.88(0.025)	1.96 (0.42)	0.171 (0.005)	1.85 (1.2)	0.017 (0.007)	0.835(0.055) 0.865(0.045) 0.895(0.035)	1.45 (0.015)	**1**	8.3(0.3) 0.08(0.01) 1.330(0.002) 1.333(0.003) 1.343(0.003)	0.997
Solution 5									
0.28(0.01) 0.49(0.015) 0.87(0.02)	2.17 (0.23)	0.165 (0.0025)	**1.97**	0.024 (0.0065)	0.815(0.045) 0.85(0.035) 0.875(0.03)	**1.47**	**1**	8.5(0.30) 0.09(0.015) 1.331(0.002) 1.333(0.003) 1.344(0.003)	1.028

AMTD
5, 6083–6145, 2012

Table 3. Aerosol and cloud retrieved parameters and associated uncertainties or min and max values [] obtained for various inversion schemes in case of a dust layer located above liquid clouds. The cloudy area is shown in Fig. 2a. The parameters that are not adjusted during the retrieval process are indicated in bold. ε is the mean square error term calculated between the measured and simulated polarized radiances.

$\tau(\lambda)$ 865 nm –> 490 nm	α	$r_{\text{eff\_f}}$ (µm)	$r_{\text{eff\_c}}$ (µm)	m_i	$\omega_0(\lambda)$ 865 nm –> 490 nm	m_r	Shape (SF)	$r_{\text{eff\_cld}}$ (µm) $v_{\text{eff\_cld}}$ $m_{r\text{-cld}}(\lambda)$ 865 nm –> 490 nm	ε $\times 10^3$
				Solution 1*					
1.17(0.15) 1.26(0.13) 1.33(0.12)	0.3 (0.9)	0.36 (0.07)	7.53 (6.5)	**0.001**	0.96(0.017) 0.95(0.02) 0.94(0.025)	**1.47**	[0; 0.13]	12.2(1.4) 0.09(0.035) 1.328(0.003) 1.333(0.005) 1.340(0.003)	0.887
				Solution 2*					
1.13(0.12) 1.23(0.1) 1.29(0.095)	0.31 (0.75)	0.40 (0.07)	8.26 (7.8)	[0; 0.001]	0.979(0.007) 0.976(0.0085) 0.970(0.011)	**1.47**	[0; 0.12]	12.1(1.4) 0.10(0.037) 1.329(0.004) 1.333(0.005) 1.340(0.003)	0.877
				Solution 3*					
1.08(0.17) 1.19(0.15) 1.27(0.15)	0.4 (1.1)	0.47 (0.12)	[0; 7.6]	[0; 0.0045]	0.96(0.07) 0.95(0.08) 0.94(0.09)	1.41 (0.035)	[0.0; 0.3]	12.4(1.6) 0.09(0.039) 1.329(0.004) 1.333(0.005) 1.340(0.004)	0.900
				Solution 4*					
1.05(0.07) 1.15(0.065) 1.26(0.075)	0.35 (0.5)	0.30 (0.045)	**2.55**	0.0007 (0.000035)	0.978(0.002) 0.981(0.0025) 0.984(0.003)	**1.47**	0.11 (0.07)	12.3(1.46) 0.11(0.036) 1.329(0.003) 1.333(0.005) 1.341(0.003)	0.950

AMTD
5, 6083–6145, 2012

Table 4. Aerosol and cloud retrieved parameters and associated uncertainties or min and max values [] retrieved with solution 5 for various situations and with solution 4* for the case related to a dust layer located above clouds. The parameters that are not adjusted during the retrieval process are indicated in bold. ε is the mean squared error term calculated between the measured and simulated polarized radiances.

$\tau(\lambda)$ at 865 nm	α	$r_{\text{eff\_f}}$ (µm)	$r_{\text{eff\_c}}$ (µm)	m_i	ω_0 at 865 nm	m_r	Shape ratio	$r_{\text{eff\_cld}}$ (µm) $v_{\text{eff\_cld}}$ $m_{r\text{-cld}}$ at 865 nm	ε $\times 10^3$
Case 1: case study with biomass burning aerosols acquired on 4 August 2008, with few aerosols above clouds (see Fig. 1a, box 2) (solution 5)									
0.063 (0.004)	1.80 (0.48)	0.148 (0.006)	**1.97**	[0; 0.0055]	[1; 0.93]	**1.47**	**1**	9.21(0.13) 0.045(0.005) 1.341(0.001)	1.584
Case 2: a very clear case with only liquid clouds; far away from continental sources of aerosols, acquired on 18 August 2008 (solution 5)									
0.022 (0.003)	0.88 (1.08)	0.19 (0.023)	**1.97**	[0; 0.013]	0.9 (0.1)	**1.47**	**1**	10.67(0.12) 0.0087(0.0015) 1.329(0.001)	0.958
Case 3: case study on mineral dust particles above clouds acquired on 4 August 2008 (see Fig. 3a, box 4) (solution 4*)									
0.61 (0.03)	0.05 (0.33)	0.19 (0.039)	**2.55**	0.00120 (0.00005)	0.967 (0.001)	**1.47**	[0; 0.03]	8.54(0.29) 0.046(0.008) 1.328(0.002)	1.268

AMTD
5, 6083–6145, 2012

Table 5. Comparisons between the droplet effective radii (r_{eff_cld}) retrieved with MODIS and POLDER and associated uncertainties for POLDER (±). Scenes with aerosols above clouds ($0.06 < \tau < 1.05$) and a cloudy scene observed in pristine conditions (τ of about 0.02).

	Dust 25 Jul 2008	Biomass 4 Aug 2008	Biomass 4 Aug 2008	Clear case 18 Aug 2008
τ at 0.865 µm	1.05 (±0.07)	0.28 (±0.01)	0.063 (±0.004)	0.022 (±0.003)
MODIS r_{eff_cld} (µm)	12.1	9	10.3	12.9
POLDER r_{eff_cld} (µm)	12.3 (±1.5)	8.5 (±0.3)	9.21(±0.13)	10.7 (±0.12)

AMTD
5, 6083–6145, 2012

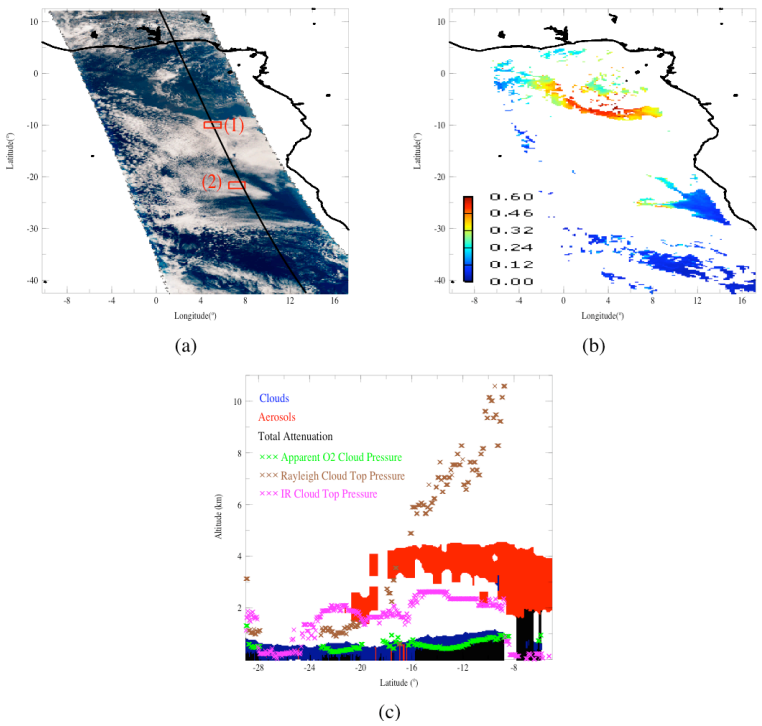

Fig. 1. A case study on biomass burning aerosols related to 4 August 2008 acquired over the tropical southeast part of the Atlantic Ocean. RGB composites of POLDER/PARASOL measurements in total radiance and lidar CALIOP track (black line) **(a)**. Total aerosol optical thickness retrieved by POLDER at 0.865 µm using the operational algorithm developed for ocean cloud-free scenes **(b)**. Vertical distribution of the cloud and aerosol layer structures derived from the CALIOP measurements (VFM products) and different estimations of the cloud top height retrieved using passive remote sensing techniques (crosses), as a function of latitude **(c)**.

AMTD
5, 6083–6145, 2012

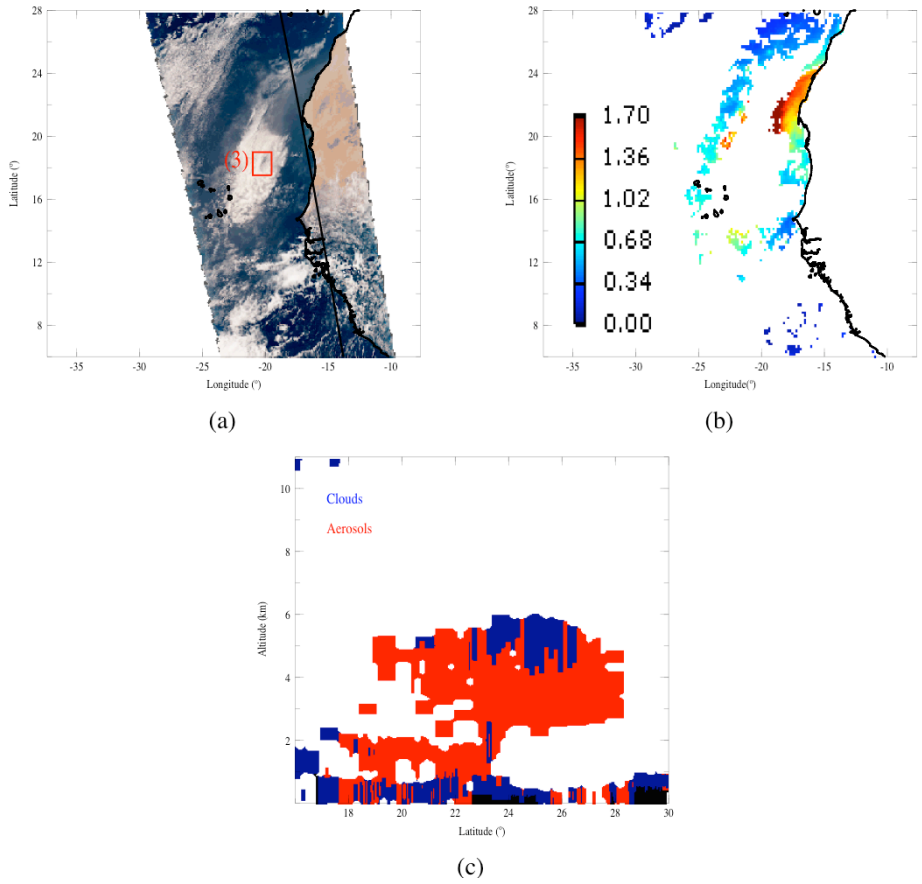

Fig. 2. Case study on mineral dust particles related to the 25 July 2008 acquired over the tropical northeast part of the Atlantic Ocean. Same figures type as the ones shown in Fig. 1. The cloud top heights retrieved with passive methods are not reported here since the cloud observed by POLDER is outside the CALIOP track.

AMTD
5, 6083–6145, 2012

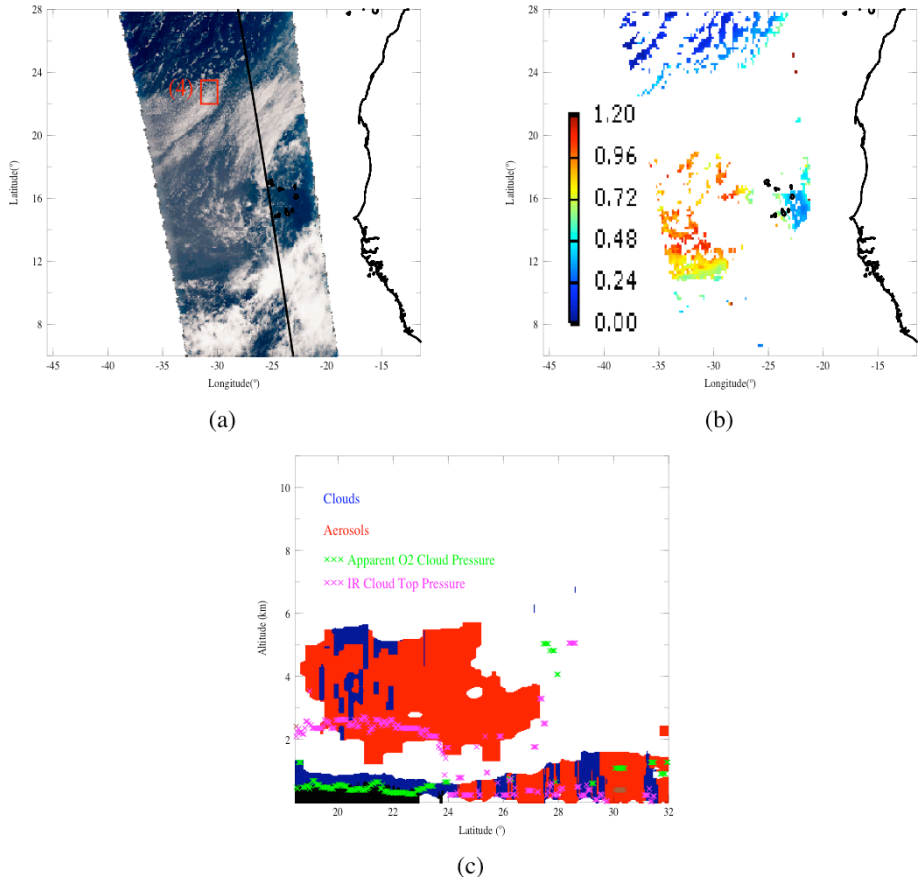

Fig. 3. Case study on mineral dust particles related to the 4 August 2008 acquired over the tropical northeast part of the Atlantic Ocean. Same figures as in Figs. 1 and 2. The so-called "Rayleigh cloud top pressure" is not available for this case due to unfavorable geometric conditions.

AMTD
5, 6083–6145, 2012

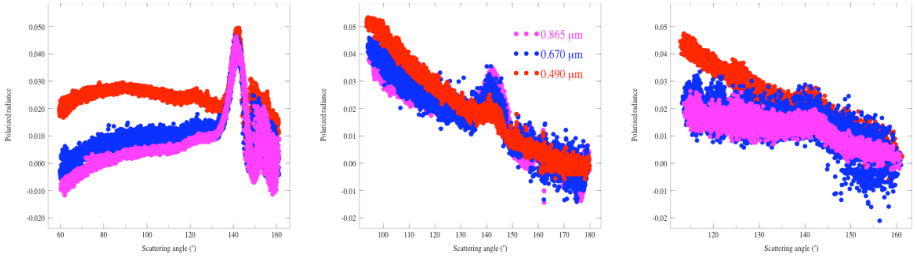

Fig. 4. Polarized radiances measured by PARASOL as a function of the scattering angle where only liquid low-clouds are present **(a)** and where a significant load of biomass burning **(b)** and mineral dust **(c)** were detected above the liquid clouds. The red, blue and magenta dots correspond to the wavelengths 0.49, 0.67 and 0.865 µm, respectively.

AMTD
5, 6083–6145, 2012

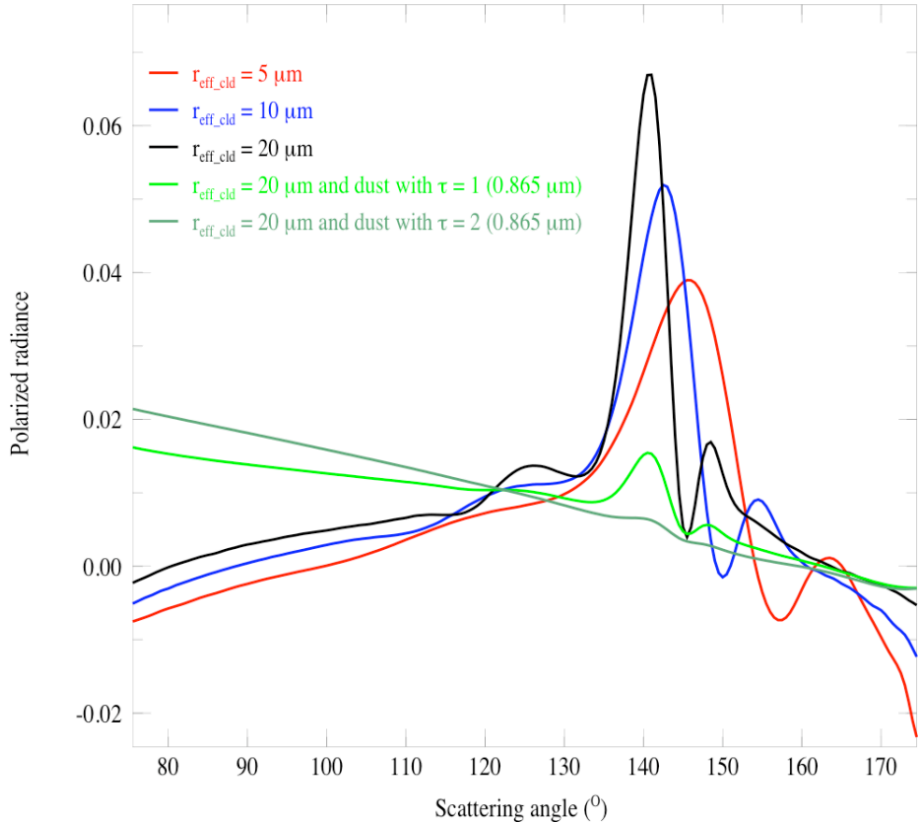

Fig. 5. Polarized radiances simulated at 0.865 µm for liquid clouds as a function of the scattering angle. Three droplets effective radii are considered (r_{eff_cld} = 5, 10 and 20 µm). Additional simulations performed with mineral dust particles suspended above liquid clouds for two aerosol optical thicknesses (τ = 1 and 2). The droplets effective radius of the cloud layer located below the aerosol layer is equal to 20 µm and the cloud optical thickness is equal to 5 for all calculations.

AMTD
5, 6083–6145, 2012

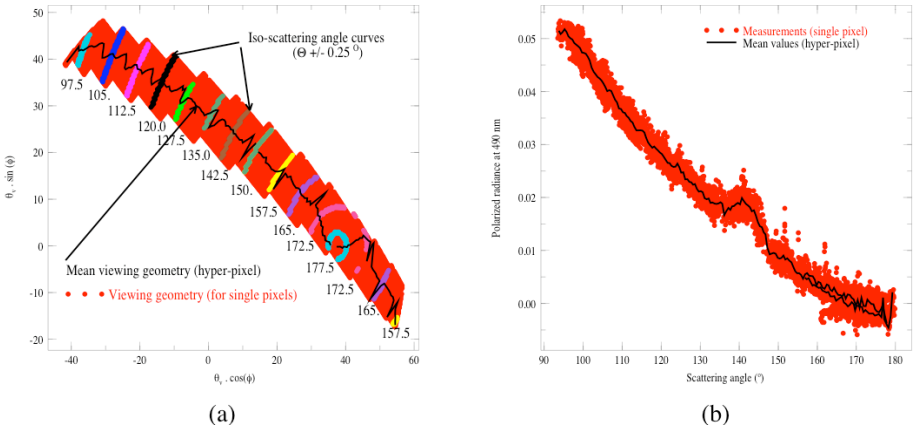

Fig. 6. Viewing geometry represented in polar coordinates for each single pixel of 6 km × 6 km (red dots) observed by POLDER within an area of 200 × 200 km^2 (the "hyper-pixel") **(a)**. The mean viewing geometry for the hyper-pixel is the black line. Polarized radiances measured for each single pixel (red dots) and mean polarized radiance for the hyper-pixel (black line) **(b)**.

AMTD
5, 6083–6145, 2012

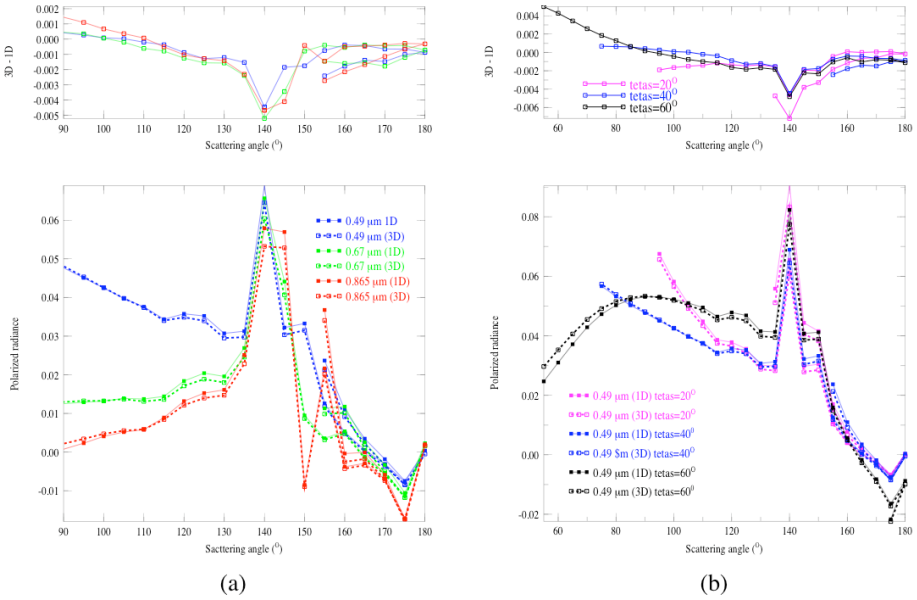

Fig. 7. 1-D vs. 3-D simulations of the polarized radiance for a liquid cloud for 3 wavelengths **(a)** and 3 different sun angles **(b)**. Dashed lines for 3-D calculations and solid lines for 1-D calculations. The red, green and blue lines in **(a)** correspond to the wavelengths 0.865, 0.670 and 0.490 µm and a sun zenithal angle of 40°, whereas the blue, black and magenta lines in **(b)** correspond to sun zenithal angles of 20, 40 and 60° and to the wavelength 0.49 µm. The absolute differences between the 3-D and 1-D calculations are shown in the upper figures.

AMTD
5, 6083–6145, 2012

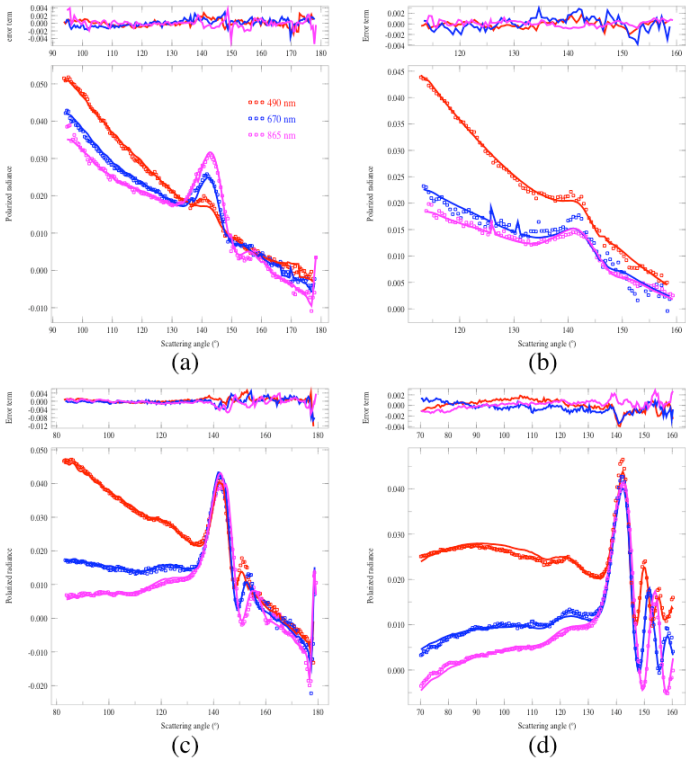

Fig. 8. Simulated and measured polarized radiance (for hyper-pixel data) for various cases: biomass burning aerosols above clouds **(a)**, mineral dust aerosol above clouds **(b)**, with few biomass burning particles above clouds **(c)** and only liquid clouds far away from the sources of aerosols **(d)**. The red, blue and magenta lines are the simulations performed at 0.49, 0.67 and 0.865 µm whereas the dots are the measurements. The upper figures show the absolute differences between measured and simulated polarized radiances.

AMTD
5, 6083–6145, 2012

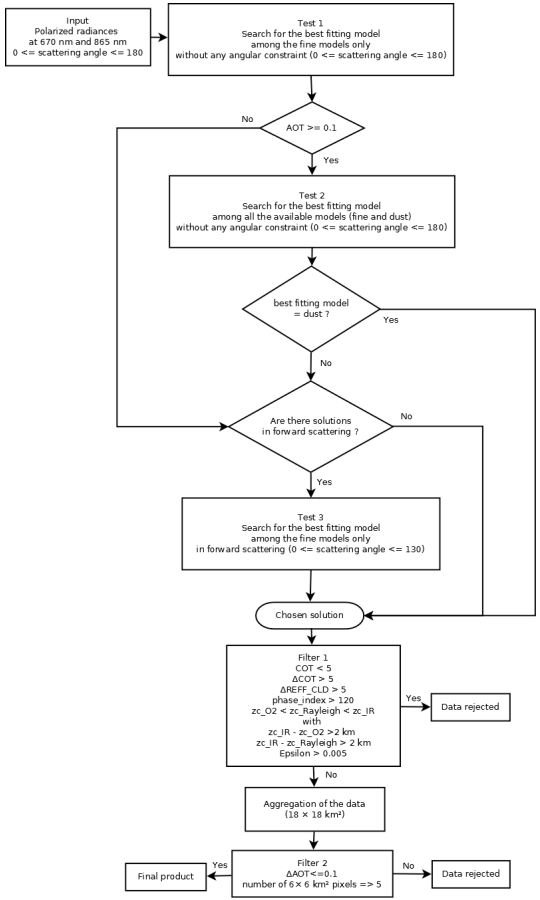

Fig. 9. Schematic view of the algorithm used to retrieve the aerosol properties above clouds from POLDER polarization data acquired at 0.67 and 0.865 µm and MODIS/POLDER combined cloud products.

AMTD
5, 6083–6145, 2012

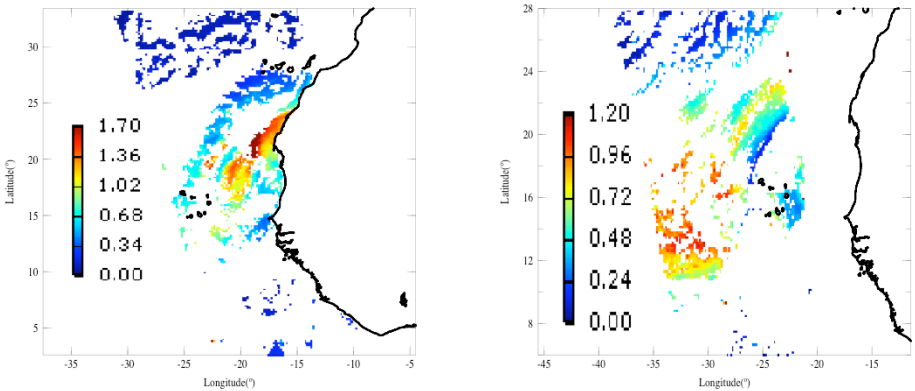

Fig. 10. Total optical thickness retrieved by POLDER at 0.865 µm over both cloud-free ocean scenes and cloudy scenes, for the case studies on mineral dust particles acquired on the 25 July 2008 **(a)** and on the 4 August 2008 **(b)**. The cloudy structures are visible in Figs. 2a and 3a for the 25 July 2008 and for the 4 August 2008, respectively. The corresponding total aerosol optical thickness retrieved only for cloud-free scenes is shown in Figs. 2b and 3b, for the 25 July 2008 and for the 4 August 2008, respectively.

AMTD
5, 6083–6145, 2012

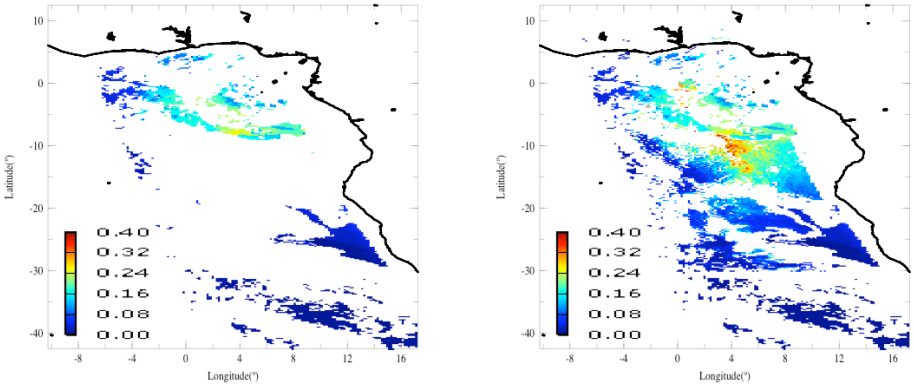

Fig. 11. Fine mode optical thickness of scattering ($\tau_f \times \omega_{0_f}$) retrieved by POLDER at 0.865 µm over cloud-free ocean scenes **(a)** and over both cloud-free and cloudy scenes **(b)**. The cloudy structures are visible in Fig. 1a. The corresponding total aerosol optical thickness retrieved only for cloud-free scenes is shown in Fig. 1b.

AMTD
5, 6083–6145, 2012

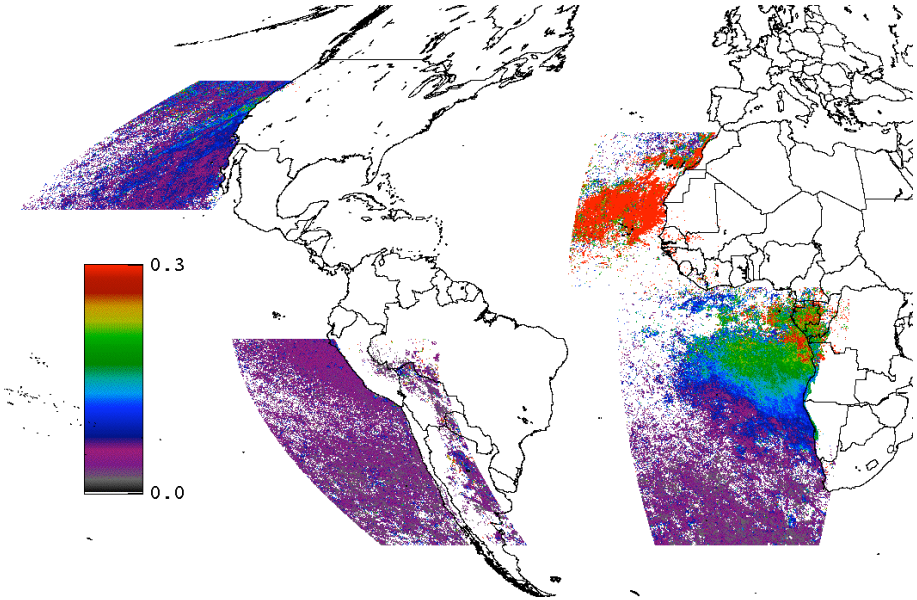

Fig. 12. Aerosol optical thickness at 0.865 µm retrieved above clouds by POLDER for four areas. Mean values computed over 3 months (June, July and August 2008).

AMTD
5, 6083–6145, 2012

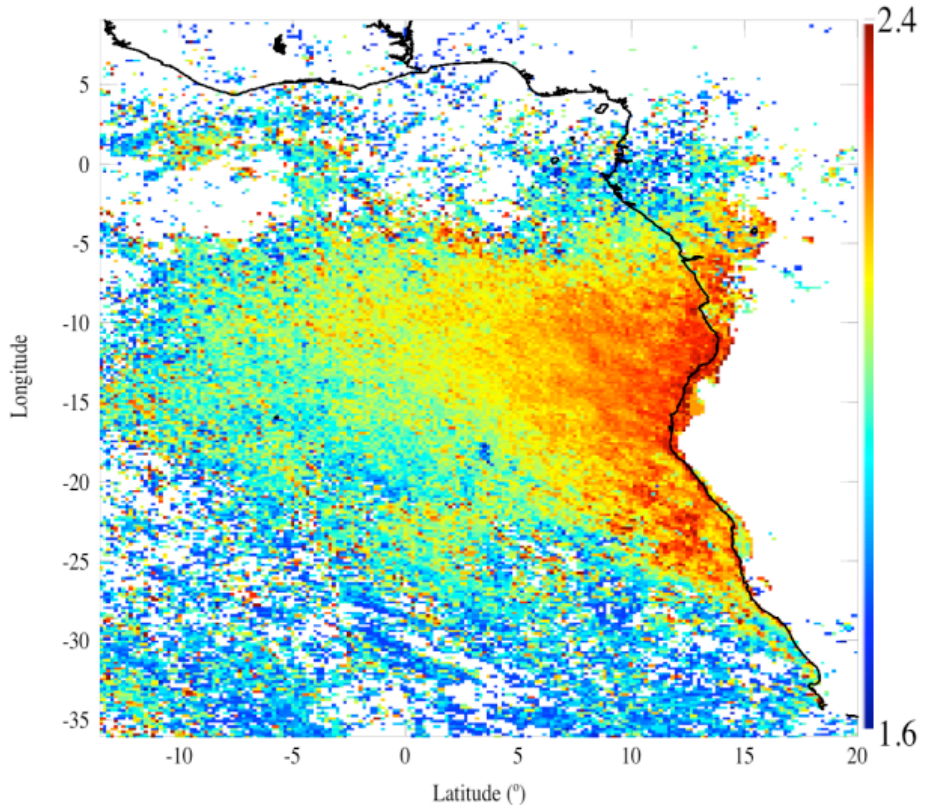

Fig. 13. Angström exponent retrieved above clouds by POLDER/PARASOL In the South Atlantic ocean near South Africa. Mean values computed over 3 months (June, July and August 2008).

AMTD
5, 6083–6145, 2012